NTNU
Norwegian University of
Science and Technology

Numerical Simulation of Viscous Flow and Use of Turbulence Models

Henrik Stumberg Larssen

Submission date: December 2017
Supervisor: Professor Bjørnar Pettersen

Norwegian University of Science and Technology, Trondheim
Department of Marine Technology

NTNU
Norges teknisk-naturvitenskapelige universitet
Institutt for marin teknikk

PROSJEKTOPPGAVE I MARIN HYDRODYNAMIKK

HØST 2017

FOR

Stud.techn. Henrik Stumberg Larssen

Numerisk simulering av viskøs strømning og bruk av turbulensmodeller
(NUMERICAL SIMULATION OF VISCOUS FLOW AND USE OF TURBULENCE MODELS)

Kandidaten skal i prosjektoppgaven sette seg inn i bruken av OpenFOAM ved å gjøre simuleringer av strømning omkring en sirkulær sylinder ved lavt Reynoldstall. Strømningsparametere, numeriske parametere, grensebetingelser, osv, kan varieres. Her skal gridgenering, løsning og visualisering også demonstreres. Dette danner bakgrunnen for videre studier av strømning omkring tredimensjonale legemer ved høye Reynoldstall i masteroppgaven til våren.
Så langt tiden strekker til, kan eksperimentering med OpenFOAM omfatte beregning av strømning rundt en tredimensjonale sirkulær sylinder. Det legges vekt på at det samtidig opparbeides erfaring med gridgenerering og visualisering.

Det skal gjennomføres et litteraturstudie rundt bakgrunn og prinsippene for bruk av turbulensmodeller, gjerne i et historisk perspektiv og med anbefaling til bruksområder, f.eks strømning omkring bluff bodies med separasjon.

Det forutsettes at Institutt for marin teknikk, NTNU, fritt kan benytte resultatene i sitt forskningsarbeid, da med referanse til studentens arbeid.

Besvarelsen redigeres mest mulig som en forskningsrapport med resymé, konklusjon, litteraturliste etc. Ved utarbeidelsen av teksten skal kandidaten legge vekt på å gjøre den så kort, oversiktlig og velskrevet som mulig.

Besvarelsen leveres i to eksemplar innen 15. desember 2017.

Bjørnar Pettersen
Professor

Faglig veileder: PhD stipendiat Håkon Strandenes

Preface

This report presents work performed during the fall of 2017 in the course TMR4520 - Marine Hydrodynamics, Specialization Project (7.5 Credits) at NTNU, Trondheim. The work has been carried out individually.

The scope of this work has been to investigate the flow around a 2D and 3D cylinder at Reynolds numbers 100 and 300, respectively. The main focus has been on developing experience with grid generation, post-processing and OpenFOAM usage. The 2D and 3D results have been compared with reference values. The rather educational aim of this project is due to the master thesis I am to write during the spring of 2018. Then, I will study the flow around some bluff body, with particular emphasis on turbulence modelling. Hence, this project also includes a minor literature study on turbulence models suitable for high Reynolds number bluff body flows. This combination of numerical simulations and turbulence modelling has been very interesting and I look forward to the thesis work in spring.

The pre-proccesing has been the most time-consuming part of the work, and there has been a few bumps along the way. Some of these mistakes have been rather silly in hindsight, but they are also part of the preparation for the thesis work. All simulations have been run on my personal computer.

Several people have contributed to this report. Most importantly, my supervisor Professor Bjørnar Pettersen has provided lots of support and motivation during the semester. He also devised a project, where I was able to more or less select a task of my own choosing. I would also like to thank Associate Professor Håvard Holm for his help with mesh generation. PhD candidate Håkon Strandnes has been helpful in troubleshooting and with explaining some OpenFOAM features. Lastly, I would like to thank Professor Bernhard Müller for CFD guidance and literature recommendations.

Trondheim, December 15. 2017

Henrik Stumberg Larssen

Abstract

In this project, numerical simulations of the external flow around a circular cylinder at Reynolds numbers 100 and 300 have been performed using OpenFOAM v1706. The simulation at $Re = 100$ is 2D, while the simulation at $Re = 300$ is 3D. The inflow condition is uniform flow in both cases. For the 2D simulation, the numerical grid has been incrementally developed through post-processing. An extensive grid refinement study has not been performed. In the 3D case, insufficient time and computer resources limited the possibility of a similar mesh verification as in 2D. The 2D and 3D results were both compared to references.
The aim of the two analyses is to obtain experience and understanding of pre-processing, post-processing and OpenFOAM usage. Hence, the accuracy emphasis is limited in the two simulations, and especially so in the 3D case. The main purpose of this project is preparation to my masters thesis work in the spring of 2018. More specifically, I aim to analyze some bluff body at high Reynolds number. With that aim in mind, the project also includes a literature review of turbulence modelling of bluff bodies at high Reynolds number. This review focuses on models suitable for engineering purposes.

In the first section of the report, the objectives and limitations of the numerical simulations and the literature review are further elaborated. Next follows a Reader's Guidance that explains the overall structure of the report. In the conclusions and further work sections, the discussion is directed towards areas within pre-processing, OpenFOAM usage, post-processing and turbulence modelling that requires further attention during the master thesis work.

The 2D simulations provided results that showed good agreement with references. Drag- and lift-coefficients, Strouhals number and separation angle were all close to reference values(within the accuracy of read off error). Also secondary flow features has been investigated, e.g. reattachment, which resulted in an estimate far from references. Due to limited accuracy in the literature review, a proper assessment of the accuracy of the simulations were unfeasible. Hence, a proper literature review and a following more rigorous convergence study are identified as future steps towards a more accurate solution.
The 3D simulations are greatly effected by a set of unphysical boundary conditions: no gradients in the cylinder length-direction at its ends. This was enforced to decrease the computational domain, and 3D effects proved to still be apparent. Values of Strouhals number and drag- and lift coefficients deviated significantly from reference values, which I assume is caused by the boundary conditions. Thus, the results were mainly used to investigate 3D separating flows in general and to learn their post-processing. In that regard, the lambda2 method was used to identify the temporal and spatial evolution of coherent flow structures. The pressure-lambda2 interdependence was also investigated. The correlation length of the coherent structures seems to be in accordance with references.
The turbulence review indicates that isotropic RANS models as $k - \omega$ and $k - \epsilon$ are unable to predict three-dimensional separating flows. It was found that EARSM, an anisotropic RANS-based model, provides significantly better predictions than the isotropic models at a limited increase in computational cost. The degree of accuracy was found to further increase with hybrid RANS-LES methods as DES and SAS. Presently, LES seems to remain to costly for engineering purposes in the prediction of high Reynolds number separating flows. That leaves EARSM, DES and SAS as suitable engineering models for the calculation of turbulent flows around bluff bodies at high Reynolds numbers.

Overall, the work with this project has provided me with a decent background in pre-processing, post-processing and OpenFOAM usage. The literature review discovered interesting results regarding the ability of different models to predict high Reynolds number separating flows. Presently, the plan for the master thesis is to perform a validation study of some of the identified turbulence models. With that aim in mind, considerable work is needed to attain the required pre-and post-processing skills and OpenFOAM proficiency. Specifically, the standardized convergence procedures require substantial pre- and post-processing efforts. Additionally, a better theoretical understanding of the identified turbuelnce models and their known deficiencies are needed. However, I think it will be very interesting and rewarding, and I consider the project as good preparation.

Contents

Project Description(Norwegian) **i**

Preface **ii**

Abstract **iii**

Nomenclature **vi**

1 Introduction **1**
1.1 Objectives and Limitations . . . 2
1.1.1 2D Simulations . . . 2
1.1.2 3D Simulations . . . 2
1.1.3 Literature Review . . . 2
1.2 Reader's Guidance . . . 2

2 Background Theory **3**
2.1 The Incompressible Navier Stokes Equations . . . 3
2.2 Boundary Layer Theory . . . 3
2.3 Flow around a Circular Cylinder . . . 4
2.4 Reynolds-averaged Navier-Stokes Equations . . . 6
2.5 Turbulent Boundary Layer Theory . . . 7
2.6 RANS Turbulence Modelling . . . 7
2.7 Large Eddy Simulations and Detached Eddy Simulations . . . 9
2.8 Computational Fluid Dynamics with the Finite Volume Method . . . 9

3 Method **11**
3.1 2D Simulations . . . 11
3.2 3D Simulations . . . 13

4 Reference Values **14**
4.1 2D Simulations . . . 14
4.2 3D Simulations . . . 14

5 Results **15**
5.1 2D Simulations . . . 15
5.2 3D Simulations . . . 20

6 Discussion **25**
6.1 2D Simulations . . . 25
6.2 3D Simulations . . . 26

7 Turbulence Modelling for Flows around Bluff Bodies **28**
7.1 The Workshop on Numerical Ship Hydrodynamics 1980-2010 . . . 28
7.2 Turbulence Modelling of Bluff Bodies . . . 29
7.3 Discussion and Recommendations . . . 32

8 Conclusions **33**

9 Further Work **34**

10 Appendix **37**
10.1 Miscellaneous Discussions . . . 37
10.2 OpenFOAM Boundary and Initial Conditions . . . 38
10.3 Boundary Layer Profiles Task A . . . 39
10.4 Top Boundary Streamwise Velocity Task B . . . 40
10.5 Pressure Contours Task C . . . 41
10.6 Final Grid Task C . . . 42
10.7 Mesh Verification Step 1 . . . 43
10.8 Postprocessing Script post.py . . . 44

List of Figures **47**

List of Tables **47**

Nomenclature

$\boldsymbol{\sigma'}$	Viscous stress tensor of Newtonian fluid in tensor notation
$\boldsymbol{\sigma}$	Stress tensor of Newtonian fluid in tensor notation
ϵ	Turbulent disspation rate
κ	Turbulent length scale wavenumber, von Kármán constant
λ_2	λ_2 in the lambda2 method
μ_t	Dynamic eddy viscosity
ν_t	Kinematic eddy viscosity
ω	Specific disspation rate of turbulent kinetic energy
ω_i	Vorticity in index notation, $(\nabla \times \boldsymbol{u})_i$
σ'_{ij}	Viscous stress tensor of Newtonian fluid in index notation
σ_{ij}	Stress tensor of Newtonian fluid in index notation
τ_w	Wall shear stress
τ_{ij}	Reynolds stress tensor in index notation
$\mathbf{f}$	Body force vector field
$\mathbf{n}$	Unit normal vector
$\mathbf{t}$	Traction vector field
$\mathbf{u}$	Instantaneous velocity in vector notation
$\mathbf{x}$	Position vector in vector notation
θ	Cylinder angle measured from mean stagnation point
θ_{reat}	Cylinder angle at reattachment
θ_{sep}	Cylinder angle at flow separation
C'_D	Drag coefficient maximum
C_L	Lift coefficient
C'_L	Lift coefficient maximum
C_s	Smagorinsky constant
C_μ	Prandtl-Kolomogorv relation constant
C'_{D_d}	Dynamic drag coefficient maximum
$C_{D_{rms}}$	Drag coefficient root mean square
C'_{D_s}	Static drag coefficient maximum
C_D	Drag coefficient
$C_{L_{rms}}$	Lift coefficient root mean square
CFL	Courant-Friedrichs-Lewy number, $\Delta t \frac{u_i}{\Delta x_i}$

$E(\kappa)$	Energy spectral density
f_i	Body force index notation
f_v	Vortex shedding frequency
k	Turbulent kinetic energy
L	Characteristic length scale
l_{mix}	Turbulent mixing length
N	Number of grid cells
P	Mean static pressure
p	Instantaneous static pressure
q	Computation time metric
Re	Reynolds number, $\frac{UL}{\nu}$
S_{ij}	Mean strain rate tensor in index notation
St	Strouhals number
u, v, w	Instantaneous velocity components in x,y,z directions
U_∞	Freestream velocity
U_i	Mean velocity in index notation
u_i	Instantaneous velocity in index notation
u_i'	Fluctuating velocity in index notation
u_*	Friction velocity, $\sqrt{\frac{\tau_w}{\rho}}$
x, y, z	Cartesian coordinates
2D	Two-dimensional
3D	Three-dimensional
Δ	LES Filter width
δ	Boundary Layer thickness at 99% of freestream velocity
δ_{ij}	Kronecker delta
δ_{sep}	Boundary layer thickness at separation
η	Kolmogorov length scale
λ	Lamé's first parameter
μ	Dynamic viscosity
ν	Kinematic viscosity
ρ	Density
B	Constant in law of the wall
u^+	Dimensionless velocity in the law of the wall, $\frac{u}{u_*}$
y^+	Dimensionless length in the law of the wall, $\frac{u_* y}{\nu}$

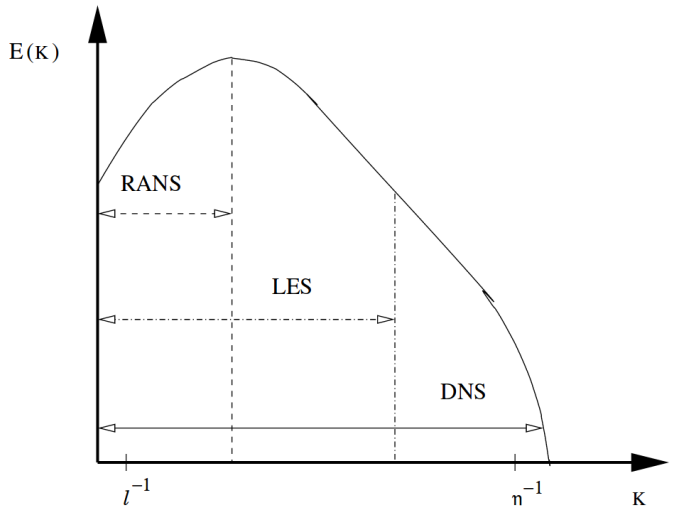

Figure 1: Energy spectrum of turbulent flow in log-log scales, figure 2.15 from Müller (2017)

1 Introduction

In everyday life we are surrounded by fluid flows, ranging from a wind gust to a ship wake. What these natural flows have in common is their chaotic behaviour. This behaviour, or flow regime, is termed turbulence. Due to its complexity, it is easy to regard turbulence as simply chaos. However, as turbulence is so common, understanding and prediction of turbulent flows are vital in a multitude of engineering fields. Marine engineering is a good example, where essentially all flows are highly turbulent.
The first pioneer in turbulence research was Osborne Reynolds. He started a systematic study of different flow regimes in the late 19th century and made vital contributions to the understanding of turbulence. After Reynolds the study of turbulence intensified, and in 1941 Andrei Kolmogorov presented his famous theory, stating that the turbulence length scales have a lower limit (Kolmogorov, 1941). In figure 1, the energy content of a typical flow is presented in wave number space κ.
It can be shown that to resolve the flow to its smallest scale, the Kolmogorov scale, the required number of grid cells in a 3D simulation is given as $N \sim Re^{\frac{9}{4}}$. In academia, flows are solved down to the Kolmogorov scale with Direct Numerical Simulations(DNS). For marine applications one may have $Re = 10^8$, resulting in infeasibly large simulations. One way to reduce the computational cost is to model the effect the smaller scales have on the larger ones. This introduces a new problem: which scales are important and how are the effect of the disregarded scales to be modelled? In figure 1, the range of scales resolved for the different approaches are indicated. What approach to use is a compromise between accuracy and computational cost. In the literature review in section 7, I will address this problem in the case of high Reynolds number flows around bluff bodies. I.e., to identify efficient turbulence models for these kind of flows for engineering purposes.

To predict a turbulent flow, the flow equations needs to be solved acurrately. This is done numerically, and is the discipline of Computational Fluid Dynamics (CFD). CFD codes are maturing after pioneering work in the 60s-80s, but it is still relatively challenging to perform accurate CFD simulations. It requires understanding and experience to make a proper numerical grid. To interpret the results, experience with post-processing and sound physical insight is needed. For advanced applications, insight into the numerical schemes are also required. In the 2D and 3D simulations of the circular cylinder, I will work towards the above goals. As OpenFOAM is open-source and correspondingly transparent and easy to modify, this software is ideal to gain insight into the numerical schemes. Hence, this part of the project is purely educational.

As aforementioned, the two threads pursued in this project, turbulence modelling and CFD simulations, will be continued in my master's thesis in the spring of 2018. Then, I will investigate the turbulence modelling of a more complicated object. Towards that end, a good understanding and some experience with CFD and turbulence modelling are essential to produce accurate results.

1.1 Objectives and Limitations

1.1.1 2D Simulations

The first part of this project concerns the CFD analysis of a 2D circular cylinder in uniform flow. The analysis is to be performed at $Re = 100$. The goal of this analysis is to gain experience with grid generation and post-processing tools to a degree, where I will be able to reproduce reference values for Strouhal number and drag- and lift coefficients within reasonable accuracy(cf. sections 2.3 and 6.1). Additionally, I will investigate separation, reattachment and other interesting flow features. This part will work as a primer for the more advanced analyses that are to be performed in the 3D simulations. With that educational aim in mind, it is limited emphasis on obtaining highly accurate results. Hence, the grid convergence studies performed in A,B and C are far from rigorous. Thus, the degree of accuracy of the final results in task D are limited.

1.1.2 3D Simulations

The goal of this analysis is to perform a CFD analysis of a 3D circular cylinder with length 8D at $Re = 300$. At this Reynolds number the flow is truly three-dimensional, making it suitable to obtain 3D post-processing experience. The length of 8D was decided after consultation with my supervisor Professor Bjørnar Pettersen. Due to limited time, this analysis is less extensive than the 2D case. The emphasis will be towards aspects of post-processing that are distinctly 3D; I will use the lambda2 method to investigate the evolution of coherent structures (Jeong and Hussain, 2006)(cf. section 2.2 and 2.3). Additionally, drag and lift coefficients and Strouhals number are to be calculated. Due to computational restrictions, the simulation will include some unphyscial boundary conditions to limit the domain size. Thus, the results will be of poor quality quantitatively, but still be usable to train the visualization of 3D separating flows.

1.1.3 Literature Review

In this literature review, I will investigate the use of turbulence modelling in marine applications. The emphasis is on turbulence modelling for bluff bodies at high Reynolds numbers. These flows are inherently three-dimensional, making the turbulence modelling challenging (cf. section 2.6) First, I will review the historical development of turbulence modelling in the marine field in general. This is limited to an assessment of the the development in turbulence modelling in the Gothenburg workshops on numerical ship hydrodynamics (1980-2010)(Larsson et al., 2014). That works as the background for a review of the more recent developments in turbulence modelling for high Reynolds number flows around bluff bodies. I.e., I will assess the current most promising models in the context of engineering demands to accuracy and computing cost. Due to time limitations, this review is far from extensive, but rather an introduction.

1.2 Reader's Guidance

The report is split into two parts thematically: one part covering the CFD simulations of the 2D and 3D circular cylinder and one part covering the literature review of turbulence modelling for marine applications. The background sections 2.1-2.3 are in connection with the simulations of the 2D and 3D cylinder. The remaining part of the background sections are all connected to turbulence modelling, except section 2.8 regarding CFD, which is relevant for both parts. Sections 3 to 6 are the reporting of the CFD simulations, while section 7 covers the literature review. The two parts may be read independently.

2 Background Theory

2.1 The Incompressible Navier Stokes Equations

The fundamental equations of fluid motion, the Navier Stokes equations, are derived from the fundamental laws of continuum mechanics. Conservation of mass results in the continuity equation (Kundu et al., 2012)

$$\frac{\partial u_i}{\partial x_i} = 0 \tag{1}$$

Conservation of linear and angular momentum results in Cauchy's theorem (Irgens, 2008).

Theorem 1 *Given a load system $\boldsymbol{t}(\boldsymbol{x}, \boldsymbol{n})$ and $\boldsymbol{f}(\boldsymbol{x})$, there is linear and angular momentum balance iff*

$$\mathbf{t}(\mathbf{x}, \mathbf{n}) = \sigma(\mathbf{x}) \cdot \mathbf{n}, \qquad \mathbf{t}(\mathbf{x}, -\mathbf{n}) = -\mathbf{t}(\mathbf{x}, \mathbf{n}), \qquad \boldsymbol{\sigma} = \boldsymbol{\sigma}^T \tag{2}$$

$$\frac{Du_i}{Dt} = \frac{1}{\rho}\frac{\partial \sigma_{ij}}{\partial x_j} + f_i, \tag{3}$$

In order to relate the stresses to the displacement field in (3), the 1st and 2nd law of thermodynamics combined with the assumption of a Newtonian fluid results in the constitutive law

$$\sigma'_{ij} = 2\mu\epsilon_{ij} + \lambda\epsilon_{kk}\delta_{ij} \tag{4}$$

In the case of incompressible fluid, the second term equals zero. The viscous stress tensor combined with the hydrostatic term yields the full stress tensor

$$\sigma_{ij} = -p\delta_{ij} + \sigma'_{ij} = -p\delta_{ij} + 2\mu\epsilon_{ij} \tag{5}$$

If equation (5) is inserted into equation (3), the result is the incompressible Navier Stokes equations

$$\frac{\partial u_i}{\partial t} + u_j\frac{\partial u_i}{\partial x_j} = -\frac{1}{\rho}\frac{\partial p}{\partial x_i} + \nu\frac{\partial^2 u_i}{\partial x_j \partial x_j} + f_i \tag{6}$$

Equations (1) and (6) constitute an elliptic-parabolic system of PDEs, which govern 3D Newtonian incompressible fluid flow (Müller, 2017).

2.2 Boundary Layer Theory

The incompressible Navier Stokes equations may be simplified in boundary layers. The concept of a boundary layer was first introduced by Ludwig Prandtl (1904). He proposed to subdivide the flow domain into two regions, one close to the wall where viscous effects are important and one where viscous effects can be neglected (cf. fig 2). This subdivison results in a great simplification of the mathematical formulation. These simplifications occur in the asymptotic limit of $Re \to \infty$ and for streamlined bodies (Schlichting et al., 2017). I. e., for bodies with $\frac{R}{\delta} >> 1$, where R is the radius of curvature and δ is the boundary layer thickness. It can be shown by dimensional arguments that

$$\frac{\delta}{L} \sim \frac{1}{\sqrt{Re}} \tag{7}$$

In the limit of large Reynolds number, it follows

$$\frac{\delta}{L} << 1 \tag{8}$$

Given the above, the 2D incompressible Navier Stokes equations may be nondimensionalized, and in the limit of $Re \to \infty$ they may be simplified to the Prandtl Boundary Layer equations.
These equations are parabolic in the streamwise direction, which is a major simplification of the original equations. If one assumes steady state, the streamwise-momentum equation has the form

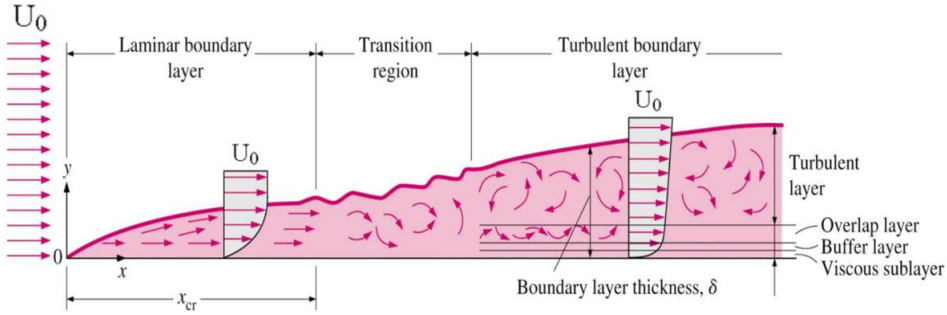

Figure 2: Boundary layer development (Çengel and Cimbala, 2013)

$$u\frac{\partial u}{\partial x} + v\frac{\partial u}{\partial y} = -\frac{1}{\rho}\frac{dp}{dx} + \nu\frac{\partial^2 u}{\partial y^2} \tag{9}$$

At the wall, (9) reduces to

$$\nu\frac{\partial^2 u}{\partial y^2} = \frac{1}{\rho}\frac{dp}{dx} \tag{10}$$

As the flow moves in the streamline direction, the pressure gradient will gradually decrease due to viscous stresses and the imposed outer potential flow. When it reaches zero(limit of an adverse pressure gradient), $\frac{\partial^2 u}{\partial y^2} = 0$, which is a necessary requirement for instability in an inviscid parallel shear flow (Drazin, 2002), the flow turns unstable. This location is a conservative estimate of stability as viscosity makes the flow more stable. Hence, as the instabilities grow and eventually explode, the boundary layer becomes turbulent(cf. figure 2). In addition to producing instabilities, the adverse pressure gradient also results in an inflection point and backflow. At an inflection point, $\frac{\partial u}{\partial y}|_{y=0} = 0$, and the boundary layer will leave the wall, resulting in an increase in the form drag.

The above discussion is limited to 2D boundary layer theory. A similar asymptotic development may be done in 3D, but the use of these boundary layer equations is quite limited and especially for separating flows. Schlichting et al. (2017) p.340 notes: "Because of the complex vortex structure arising in three–dimensional separation, a displacement correction, as is possible in plane flows and as will be described in Chap. 14 as a higher order effect, is also no longer possible. In this case, there are no further advantages to using the asymptotic theory ($Re \to \infty$) over the solution of the complete equations of motion." Thus, the three-dimensional effects make the analysis difficult, as separation will vary in the spanwise direction and make the wake vortex dynamics far more complex than in the 2D case. Usual practice in identifying these vortex structures (also termed coherent structures) is the lambda2 method (Jeong and Hussain, 2006).

2.3 Flow around a Circular Cylinder

The flow around a circular cylinder has been extensively studied since Von Kármán's seminal papers in 1912. The flow is highly dependent on the Reynolds number and for Re>40, the flow becomes unsteady and is characterized by a Von Kármán vortex street (Sumer and Fredsøe, 1997). In this phenomena, vortices are shed alternately at each side of the cylinder, resulting in a flow pattern as in figure 3. Inside a given vortex there is a low pressure region.
As mentioned in section (2.2), in boundary layers with adverse pressure gradients the boundary layer profile will leave the wall, and these flow structures (shear layers) will have high levels of vorticity. Due to the intrinsic instability of the flow, one of the vortices, e.g. A, will eventually grow stronger than the other, B, such that it drags B to A's side (cf. figure 4). B will in turn cut of vortex A. Vortex B will now push Vortex C to its side causing B to be cut. This periodic phenomena is an explanation for the primary wake mode in the flow around a 2D circular cylinder at low Re.
As Re increases the flow becomes more complex. For $Re > 180$, the flow becomes three-dimensional. I.e., the vortex shedding will vary in the spanwise direction with some length scale denoted as

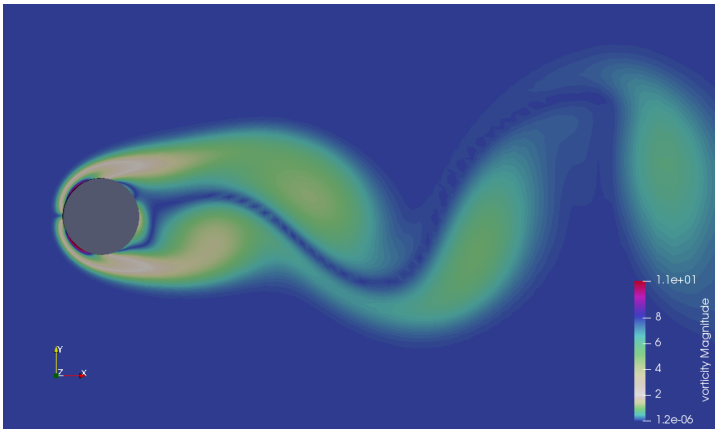

Figure 3: Von Kármán vortex street $Re = 100$, $\sqrt{\omega_i \omega_i}$

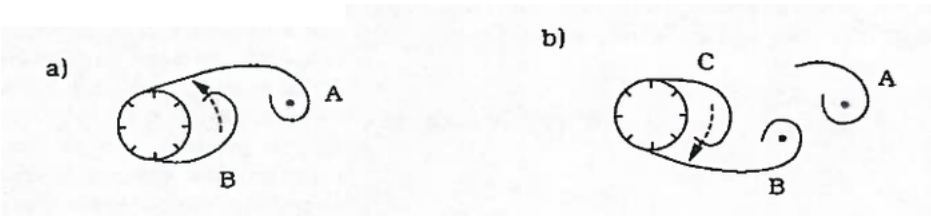

Figure 4: Vortex shedding as depicted in figure 1.7 in Sumer and Fredsøe (1997)

the correlation length. Table 1.1 in (Sumer and Fredsøe, 1997) shows the Re dependence on the correlation length. To investigate this 3D vortex shedding, it is important the cylinder has sufficient length, such that end-effects do not influence the shedding at mid-length. As Re increases, the flow becomes gradually turbulent. The transition starts downstream in the wake at $Re \sim 200$ and with increasing Re the wake and boundary layer becomes completely turbulent at $Re > 4 \cdot 10^6$.

$$St(Re) = \frac{f_v(Re)D}{U_\infty} \tag{11}$$

The primary vortex shedding frequency varies with Reynolds number only and is determined in terms of the nondimensional Strouhals number. The vortex shedding causes an asymmetric pressure field and thus a force resultant. Most significantly, the flow causes a periodic lift force, which gives rise to vortex induced vibrations. The lift force is in phase with the vortex shedding frequency, while the drag force has frequency $2f_v$. The drag force will consist of an almost steady part due to skin friction, C_{D_s}, and a dynamic part due to the form drag following the vortex shedding, C_{D_d}. The two force resultants are typically nondimensionalized to a lift and drag coefficient.

$$C_L = \frac{F_y}{\frac{1}{2}\rho U_\infty^2 D L_z}, \qquad C_D = C_{D_s} + C_{D_d} = \frac{F_x}{\frac{1}{2}\rho U_\infty^2 D L_z} \tag{12}$$

Besides the primary flow structure described above, there will also be secondary flow structures. For instance, parts of the shear layer may reattach to the cylinder. Similarly as with the the primary flow structure, these structures will be Reynolds number dependent and periodic. An important variable in explaining the flow is the separation point, which may be given as an angle in the case of the 2D cylinder, θ_{sep}. I.e., at the separation point the vortices leave the cylinder and thus determine the vortex dynamics in the wake. In the boundary layer, the wall shear stress is given as

$$\tau_w = \mu \frac{\partial u_\theta}{\partial r} \tag{13}$$

Following the definition of the separation point in section 2.2, we will have $\tau_w(\theta_{sep}) = 0$. Thus, the separation point may be found by investigating the wall shear stress of the cylinder. In addition to separation points, the wall shear stress will also equal zero at reattachment points.

2.4 Reynolds-averaged Navier-Stokes Equations

One of the more fruitful and applied approaches to turbulence modelling is the Reynolds decomposition (Wilcox, 2006). This decomposition splits the velocity field $u_i(\mathbf{x}, t)$ into two parts: a slowly varying, mean part $U_i(\mathbf{x}, t)$ and a rapidly changing, fluctuating one $u_i'(\mathbf{x}, t)$.

$$u_i(\mathbf{x}, t) = U_i(\mathbf{x}, t) + u_i'(\mathbf{x}, t) \tag{14}$$

Let the mean part have a characteristic time scale $T2$, and these variations are not turbulent in nature. Further, let $T1$ denote a timescale significantly larger than the time scales of the rapidly changing turbulent fluctuations. The mean velocity is defined as

$$U_i(\mathbf{x}, t) = \frac{1}{T}\int_t^{t+T} u_i(\mathbf{x}, t)\ dt, \qquad T1 << T << T2 \tag{15}$$

The decomposition is well depicted in figure 2.5 from Wilcox (2006) given in figure 5. If the decomposed velocity field is inserted into the momentum equation and then time averaged as in equation (15) (denoted with an overbar), the result is the Reynolds-averaged Navier-Stokes equations (RANS).

$$\frac{\partial U_i}{\partial t} + U_j\frac{\partial U_i}{\partial x_j} = -\frac{1}{\rho}\frac{\partial P}{\partial x_i} + \frac{1}{\rho}\frac{\partial}{\partial x_j}(2\mu S_{ij} - \overline{\rho u_i' u_j'}) + f_i \tag{16}$$

Compared to the Navier-Stokes equations, there is one major difference, and that is the second to last term, $\overline{-\rho u_i' u_j'}$. These 6 terms are denoted the Reynolds stresses and are collected in the Reynolds-stress tensor τ_{ij}.

$$\tau_{ij} = -\overline{\rho u_i' u_j'} \tag{17}$$

Hence, we have 6 new unknowns but no new equations. This is termed a closure problem. Thus, to close the problem the Reynolds stresses needs to be modelled in some fashion. The models applied to the Reynolds stress tensor can be subdivided into three categories: algebraic models, two/one equation models and Reynolds stress models (cf. section 2.6). For the two former ones, the Boussinesq assumption is used

$$\tau_{ij} = -\rho\overline{u_i' u_j'} = 2\rho\nu_t S_{ij} - \frac{2}{3}\rho k\delta_{ij} \tag{18}$$

Note that the kinematic eddy viscosity is a flow parameter rather than a fluid property as the regular kinematic viscosity. This relation replaces the 6 unknown Reynolds stresses with two new unknowns: ν_t and k. The relation implicitly assumes ν_t to be an isotropic scalar. This assumption is especially problematic for flow cases with anisotropic turbulence, which occur in highly curved and three-dimensional flows(Wilcox, 2006).

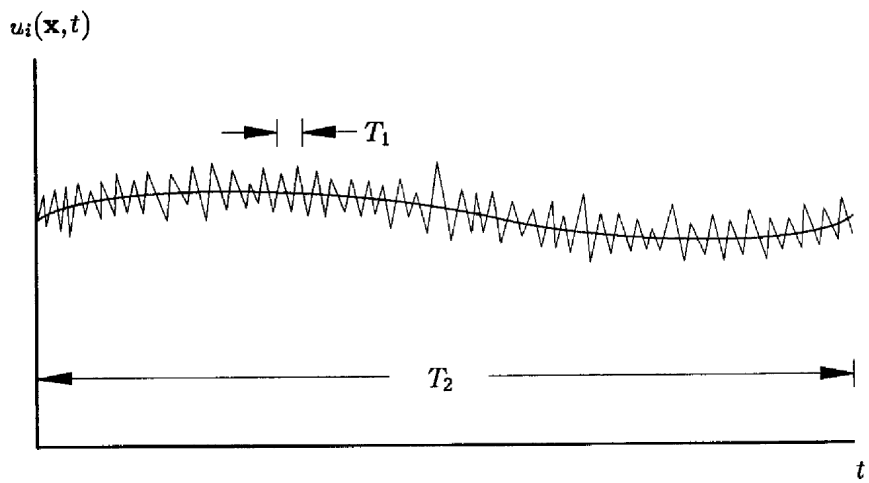

Figure 5: Time averaging of nonstationary turbulence (Wilcox, 2006)

2.5 Turbulent Boundary Layer Theory

Similarly as in the laminar case, the RANS-equations may be simplified to a boundary layer version. Alternatively, simple turbulent boundary layers may be described by the the law of the wall (Wilcox, 2006). In this case, simple translates to flows with limited curvature and no separation or reattachment. Then, based on dimensional arguments, one may assume

$$u = f_1(\rho, \tau_w, \nu, y) \tag{19}$$

After dimensional analysis, the expression reads

$$u^+ = f(y^+) \tag{20}$$

where the following nondimensional variables are used

$$u^+ = \frac{u}{u_*}, \quad u_* = \sqrt{\frac{\tau_w}{\rho}}, \quad y^+ = \frac{y}{\nu/u_*} \tag{21}$$

By physical arguments, the shape of f can be determined; closest to the wall, in the viscous sublayer, viscous effects dominate, in the mid region, the buffer layer, both viscous and Reynolds stresses are important and in the outer layer, the log layer, the Reynold stresses dominate. In the log layer, f have the form

$$u^+ = \frac{1}{\kappa} ln(y^+) + B \tag{22}$$

where κ is the Von Kármán constant and B is a constant depending on the wall surface roughness. Equation (22) is highly important as it provides a simple boundary condition for the velocity at the outer parts of the boundary layer. This contrasts to resolving the extremely small scales in the turbulent boundary layer. As aforementioned, the law of the wall does not predict separation or reattachment, making other approaches needed. In the case of RANS, specific models used for low Reynolds number flows have been developed to resolve the boundary layers. Alternatively, more costly techniques as LES may be applied (cf. section 2.7).

2.6 RANS Turbulence Modelling

RANS contains 6 unknown Reynolds stresses. Below the most important RANS turbulence models are presented in increasing degree of complexity.

Algebraic models

The simplest turbulence models are algebraic models. The Boussinesq assumption is utilized and the eddy viscosity is given as an algebraic relation dependent on the mean flow. The ease of use of these models are their main benefit. In Prandlt's mixing length model, the relation is given as

$$\mu_t = \rho |\frac{\partial U}{\partial y}| l_{mix}^2 \tag{23}$$

l_{mix} is usually proportional to the distance to the closest wall. The need to determine this mixing length is a poor property of the model. Additionally, the model does not take into account convective or diffusive effects, making it limited to simple free shear flows.

Two equation models

A more complex family of models are two equation models. In these models, two new transport equations are introduced. First, a transport equation for the turbulent kinetic energy is constructed. This equation is based on the exact equation for the turbulent kinetic energy, which can be derived by multiplying the incompressible Navier Stokes with u_i' and then perform time averaging. When constructing the model equation for k, the effect of viscous diffusion is neglected, making a special near wall treatment needed. To achieve closure, Prandtl and Kolmogorov connected ν_t and k through the Prandtl-Kolmogorov relation (may be regarded as a local mixing length model)

$$\nu_t = C_\mu \sqrt{k} L \tag{24}$$

Furthermore, one may argue that the length scale L will change in the flow domain, resulting in a new transport equation for $k^m L^n$, where m and n are integers. The two most famous examples are the dissipation of turbulent kinetic energy ϵ and the specific dissipation rate ω.

$$\epsilon = C_\mu \frac{k^{3/2}}{L}, \qquad \omega = \frac{\sqrt{k}}{L} \tag{25}$$

Transport equations are constructed for ϵ and ω, involving the most common physical processes involved in the motion of fluids: unsteadiness, convection, diffusion, dissipation and production. Hence, the equations are products of physical reasoning and dimensional analysis. Now, ν_t and k are determined and the set of equations are closed. These two models have been tested and extended through the years and some of their strengths and weaknesses have become apparent (Wilcox, 2006). The $k-\epsilon$ model has difficulty with converging close to walls and is often difficult to couple with wall functions. This makes its overall ability to calculate complex boundary layers limited. On the other hand, the $k-\epsilon$ model is easy to implement and good in the far field. The $k-\omega$ model is good close to walls and may be used without wall functions. Accordingly, it can reproduce quite complex 2D boundary layers. This model is very sensitive to free stream boundary conditions (k and ω boundary conditions), yielding poor performance in the free stream. These contrasting properties motivated the development of a combination of the two, the SST $k-\omega$ model. This model uses the $k-\omega$ model close to walls and $k-\epsilon$ in the free stream. Common to booth models is their limited accuracy for flows around curved surfaces, where the turbulence is anisotropic. This may be traced back to the Boussinesq assumption, where the eddy viscosity is assumed equal in streamwise and crossflow directions (Wilcox, 2006). Another poor property of these models is a large set of closure coefficients. These coefficients are determined through validation studies, making their accuracy correlated to the type of flow used in validation.

Reynolds stress models

The Navier-Stokes equations may be manipulated to construct transport equations for each Reynolds stress. If the equations are rewritten in the form

$$\mathcal{N}_i = 0 \tag{26}$$

The following operation results in transport equations for each Reynolds stress

$$\overline{\mathcal{N}_i u_j' + \mathcal{N}_j u_i'} = 0 \tag{27}$$

These transport equations include new unknown terms in the form $\rho\overline{u_i' u_j' u_k'}$, which require further modelling(cf. equation (2.34) in Wilcox (2006)). As each Reynolds stress has its own transport equation, there will be 6 additional PDEs to solve. Additionally, a transport equation for a turbulence quantity as ϵ or ω is needed to close the system(a scale-determining equation). Hence, RSM models are costly, since they add 7 PDEs to the equation system. At the same time, they do allow for complex turbulent flows and do not assume local isotropic eddy viscosity as in the two equation models.The RSM models are thus physically more realistic models than the two equation models and should, among others, be better at computing three-dimensional flows with curved streamlines than the two equation models. However, in practice the results often only show qualitative agreement. Wilcox (2006) finds it likely that this is connected with shortfalls in the scale determining equation. Contrary to full RSM as descirbed above, there is algebraic stress models(ASM). In ASM each Reynolds stress is determined by an algebraic expression. These relations may be implicit or explicit, and in the explicit case these models are denoted explicit algebraic stress models (EASM or EARSM). These models have showed good agreement for curved boundary layers, as the equivalent to the eddy viscosity is anisotropic (Wilcox, 2006).

2.7 Large Eddy Simulations and Detached Eddy Simulations

Large eddy simulations(LES) is an alternative to RANS. Instead of performing time-averaging, spatial averaging is performed in LES (Wilcox, 2006). The simplest type of filter is the volume-average box filter introduced by Deardorff

$$\overline{u_i}(\mathbf{x},t) = \int_{x-\frac{1}{2}\Delta x}^{x+\frac{1}{2}\Delta x} \int_{y-\frac{1}{2}\Delta y}^{y+\frac{1}{2}\Delta y} \int_{z-\frac{1}{2}\Delta z}^{z+\frac{1}{2}\Delta z} u_i(\boldsymbol{\xi},t) d\xi d\eta d\zeta \tag{28}$$

$\overline{u_i}$ denotes the resolvable-scale filtered velocity and the subgrid-scale velocity u_i' and the filter width Δ is defined by

$$u_i' = u_i - \overline{u}_i, \qquad \Delta = (\Delta x \Delta y \Delta x)^{\frac{1}{3}} \tag{29}$$

Similarily as for RANS, a continuity equation and momentum equations can be developed for the resolvable scales by performing spatial averaging. Instead of Reynolds stresses, the momentum equations include subgrid-scale Reynolds stresses τ^s. I.e., stresses due to momentum transfer from the resolvable scales to the subgrid. One of the earliest and most popular models is the Smagorinsky model, where the effect of the subgrid scale Reynolds stresses are modelled by a Smagorinsky eddy viscosity

$$\nu_t = (C_s \Delta)^2 \sqrt{S_{ij} S_{ij}} \tag{30}$$

Note the energy spectrum in figure 1; with decreasing filter width, the effect of the subgrid scales become less important as the energy and corresponding influence of the subgrid is reduced. A major problem with LES is the fine scales close to walls, where the energy bearing eddies are all small, making a LES simulation approach the required grid spacing and time step of DNS. One potential solution to this problem is Detached Eddy Simulations(DES). In DES, RANS is used to handle attached boundary layers and thin shear layers, while LES is used elsewhere in the flow domain. This approach introduces new difficulties, as where to switch between the two models. This is further discussed in Wilcox (2006). An alternative to the hybrid RANS-LES formulation is Scale-Adaptive simulation theory (SAS). This approach has the benefit of dynamically adjusting to LES-behaviour (Menter and Egorov, 2010).

2.8 Computational Fluid Dynamics with the Finite Volume Method

For the CFD simulations in this project, the Finite Volume Method(FVM) has been used. In FVM, the flow domain is discretized into finite volumes, using the integral form of the continuity, momentum equations and other transport equations(Versteeg and Malalasekera, 2007). When assessing results from a CFD simulation, it is important to note that the numerical solution is only an approximate solution to the real-world problem. The error may be split into two: discretization errors and modelling errors. The discretization errors are caused by an inexact numerical solution of the PDEs. This includes truncation errors due to approximations of derivatives, iteration errors due to iterative solutions to linear systems and rounding errors due to finite machine precision. With decreasing spatial and temporal discretization, the truncation errors will decrease, while the round-off error increase. A systematic study of discretization errors is denoted a grid convergence study and has many standardized formulations, e.g. Wang et al. (2008). The modelling errors denote the error in the mathematical model compared to the real world problem. For instance, an inaccurate turbulence model will introduce a modelling error.

In the following, the numerical schemes used in the simulations are briefly described. The spatial discretization was performed with OpenFOAM's "Gauss linear", which is 2nd order accurate for regular meshes (Jasak, 2015). The temporal discretization was "Euler", which is a first order implicit method. In this discretization, the convective fluxes are linearized, resulting in a linear system of equations at each time step. To achieve convergence, the continuity equation is used to calculate pressure and velocity corrections. In particular for these simulations, the PISO algorithm

has been utilized through OpenFOAM's pisoFoam solver(Versteeg and Malalasekera, 2007). After convergence at a given time step, transport equations are solved. In the case of standard RANS two equation models, values for k and ϵ or ω are calculated. Besides the associated truncation errors, the stability of the chosen numerical schemes are important. This particular spatial discretization may introduce oscillations, as it introduces no numerical viscosity. Regarding temporal discretization, the maximum Courant number(CFL) should be well below unity.

To be able solve the discretized equations according to the actual flow problem, correct boundary conditions must be prescribed. As noted in Versteeg and Malalasekera (2007), the pressure correction method, sets some direction for this procedure. For instance, the first pressure corrector step for the x-velocity correction at cell i,j,k in PISO is equal to a SIMPLE correction

$$u'_{i,J,K} = -d_{i,J,K}(p'_{I,J,K} - p'_{I-1,J,K}) \tag{31}$$

where $d_{i,J}$ is a constant. Therefore, if u is prescribed, the gradient of p is prescribed. In essence, the system of equations must not be overdetermined or underdetermined. In the simulations, I have used guidelines for external flows given from my supervisor Professor Bjørnar Pettersen and from Versteeg and Malalasekera (2007). In appendix 10.2, a description of boundary and initial condition specification in OpenFOAM is given.

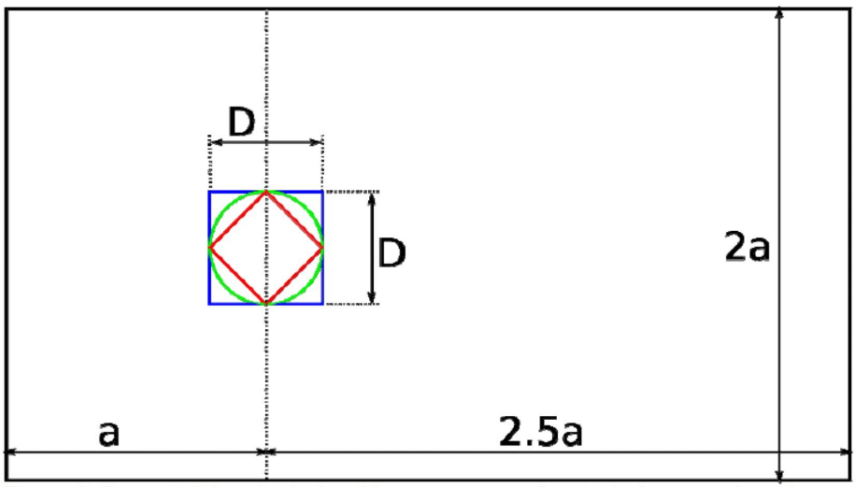

Figure 6: Flow domain 2D

3 Method

3.1 2D Simulations

Mesh Topology

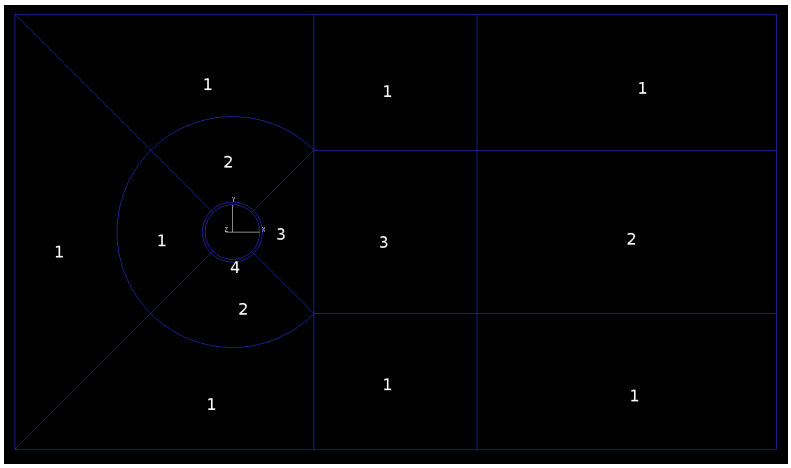

Figure 7: Mesh topology 2D

The flow domain is given in figure 6, and there is inflow from the leftmost boundary. Figure 7 shows the overall mesh topology for the 2D simulations, a C-mesh. Each patch is assigned a number, where 1 is the coarsest- and 4 the finest grid. Zone 4 is the inner boundary layer, where a fine resolution is necessary to capture the sharp velocity gradients. Zone 3 is the initial wake, where an accurate treatment is needed to resolve the vortex dynamics. The mesh was generated by the NTNU in-house meshing tool MEGA, which has been developed by Associate Professor Håvard Holm. All grids are structured with hexahedral cells. Cf. appendix 10.6 for the final grid.

Software, Fluid Properties and Boundary Conditions

OpenFOAM v17.06 was used to perform the analysis. Given the smooth flow in this problem, OpenFOAMs standard numerical schemes were used(cf. section 2.8). The boundary- and initial conditions are summarized in table 1 and are chosen based on the argument in section 2.8 and the descriptions in appendix 10.2. Note, a condition on a vector field is prescribed componentwise. The fluid properties are given as $\rho = 1000\ kg/m^3$ and $\nu = 0.02\ m^2/s$. The inflow velocity equals unity and the cylinder diameter equals two. This corresponds to $Re = 100$.

	U_{BC}	P_{BC}	U_{IC}	P_{IC}
Inflow	uniform (1 0 0)	zeroGradient		
Outflow	zeroGradient	uniform 0		
Top & Bottom	zeroGradient	zeroGradient		
Flow Domain			uniform (0 0 0)	uniform 0

Table 1: Initial- and boundary conditions 2D

Note Regarding Post-processing

In this analysis, the flow is to be investigated at steady state. Note that steady state is merely intended in a statistical manner, as the flow is periodic. I.e., at steady state the force coefficient maxima will stay constant. The flow reached this point at approximately $t = 170\ s$, so I only used data after this time instance. The post-processing has been performed using Paraview 5.4.0. Additionally, Paraview's python interface has been used to perform post-processing using python 2.7 with the script post.py (cf. appendix 10.7).

Task A

This task consists of determining the necessary grid resolution of the boundary layer. To do so, one first needs to estimate the boundary layer thickness. As a first guess, Blasius' solution for the boundary layer thickness of a flat plate was used (White, 2007). It is assumed that the boundary layer will be at its thickest at the separation point

$$\delta_{sep} \approx 3.5\sqrt{\frac{2\nu x_{sep}}{D}} \tag{32}$$

For $Re = 100$, separation occurs at $\theta \approx 118°$ (cf. section 4.1). As the boundary layer development is limited close to the stagnation point, I assumed $x_{sep} \approx \frac{\pi}{4} = \frac{D}{8}$. This inserted into (32) yields $\delta_{sep} \approx 0.44$. However, curvature will play an important role, and I assumed the Blasius solution to be a conservative estimate. I assume $\delta_{sep} \approx 0.3$ as a first estimate. To find an adequate mesh resolution in the boundary layer, I investigated the boundary layer at $\theta = 60°$ for different resolutions. This was conducted at the same time instant, $t = 158.8s$. When improving the resolution, I also adjusted the time step such that $CFL_{max} \approx 0.7$. A correctly resolved boundary layer is smooth and has converged(does not change with finer resolution). This check was performed by investigating boundary layer profiles visually. I first did the simulation with a quite fine mesh, N = 12, and this indicated that $\delta \approx 0.25$. Since the grid is quite smooth, I did not change the size of the inner boundary layer. I.e., zone 4 in figure 7.

Task B

Task B is to determine the size of the computational domain. The flow domain given in figure 6 was used, such that a needs to be determined. The boundary layer mesh from Task A shall be kept constant. I.e., the C in the mesh will stay unchanged, such that $a \gtrapprox 2.5$. The computational domain has an adequate size if an increase in domain size does not affect C'_D, C'_L or St significantly (denoted as the primary variables). Such integrated variables are insensitive to change. However, as they are easily calculated and given the objectives of these simulations (2D and 3D) they are used to study convergence. To compensate for their insensitivity, the top and bottom boundary stream-wise velocity are also investigated. This velocity should be close to the free-stream velocity, as the effect of the body should be small far away from the body. As the body causes a displacement effect, there will be some deviation from unity. Further, to calculate C'_D, C'_L and St, I used OpenFOAM's forceCoeffs functions and the python script post.py (cf. appendix 10.7). St was calculated by performing a FFT of the pressure at a numerical probe and choosing the non-zero frequency with maximum amplitude. The location of the probe proved to yield the same Strouhal number, as long as it was placed a few diameters downstream within the wake.

Task C

Before moving to temporal convergence, the grid was subjected to a final set of refinements. Throughout the grid, the pressure shall be continuous. Thus, by investigating pressure contours one may find faulty areas in the grid. Critical areas of the grid, as in the boundary layer and at the top right- and bottom right corners of the C, was investigated. When these contours seemed to be smooth in the entire flow domain, the mesh development is finished. To determine the necessary temporal discretization, the time step is gradually decreased until the primary variables converges. The coarsest usable time step is the one that just manages to keep the solution stable. Thereafter, the time step is decreased while the primary variables are monitored by use of post.py.

Task D

With converged boundary layer resolution, time step and an appropriate domain size, the solution should be quite accurate such that the flow may be studied in detail. Primary variables are calculated in post.py, while interesting screenshots were taken in ParaView. The primary variables were compared to reference values (cf. section 4.1). Furthermore, OpenFOAMs postprocessing

function wallShearStress was used to calculate the wall shear stress. This data was used to determine the separation- and reattachement points. The periodic movement of the stagnation point was examined by displaying velocity magnitude data in Paraview. Vorticity and pressure contour plots were used to clearer identify primary and secondary flow structures, and to assess the interplay between vorticity and pressure. Vorticity plots were also used to investigate reattachment. To determine the frequencies of these structures a numerical measuring probe was used. The FFT of these results provided the frequency information of the secondary flow structures.

3.2 3D Simulations

Mesh Topolgy

The 2D topology in figure 7 is the basis for the 3D mesh. As the 3D simulations are relatively costly compared to the 2D simulations, the 2D mesh is first coarsened in non-critical areas. After this operation, the mesh is extruded in z-direction the length of the cylinder. The 3D mesh topology is given in figure 16a.

Software, Fluid Properties and Boundary conditions

The software and numerical schemes used in the 2D simulations where also used in the 3D simulations. The boundary conditions in the 3D simulations are very similar to those in 2D given in table 1. To achieve $Re = 300$, the inflow velocity is changed to 3, resulting in the inflow boundary condition: uniform (3 0 0). There will be two new boundaries in the z-direction, denoted the front and back boundaries. These are similar to the top and bottom boundaries and U and p are given the same zeroGradient boundary condition. This is an unphysical boundary condition as there will be variations in z-direction at the cylinder ends. However, with a relatively long cylinder, these effects may not influence the flow at the mid-length of the cylinder. This boundary condition is chosen as it is computationally cheap compared to a wall, where a boundary layer would develop. Except for the aforementioned modifications, the boundary conditions used at the old 2D boundaries stay unchanged.

Mesh Development and Numerical Simulation

The tasks performed in the 2D simulations are ultimately steps to produce a grid with adequate quality for the objectives given in section 1.1.1. The goals are similar for the 3D mesh design. The following method aims to produce an adequately good mesh for the objectives in section 1.1.2. The starting point is the mesh used for the 2D simulations. This mesh was not computationally restrictive for the 2D simulations, so it is relatively fine compared to the objectives of the simulation. As the 3D simulations are expensive and the mesh is an extrusion of the 2D mesh, the 2D mesh is first coarsened. The coarsened mesh was checked with 2D simulations at $Re = 300$ (step 1). Next, the mesh is extruded the length of the cylinder and checked visually and with OpenFOAM's checkMesh utility. After passing the checkMesh, the 3D simulations are performed and then evaluated. If the results are purely 2D (due to grid design and/or boundary conditions), the mesh needs to be altered (step 2). When the results are three-dimensional, the results may be evaluated given the targets in section 1.1.2 and compared to the reference values in section 4.2 (step 3). To calculate the coherent structures with the λ_2 method, OpenFOAM's Lambda2 utility was used. λ_2 contours were used to investigate temporal and spatial evolution of flow structures and to investigate the pressure-λ_2 interdependence. The Strouhals number is found by averaging p in the z-direction downstream in the wake (at $(x, y) \approx (5D, -D)$). The drag-and lift coefficient maxima are found using OpenFOAM's forceCoeffs functions. The increase in CPU time from the 2D simulations has been estimated by using the metric $q = t_{simulation} * \#processors/t_{computing}$.

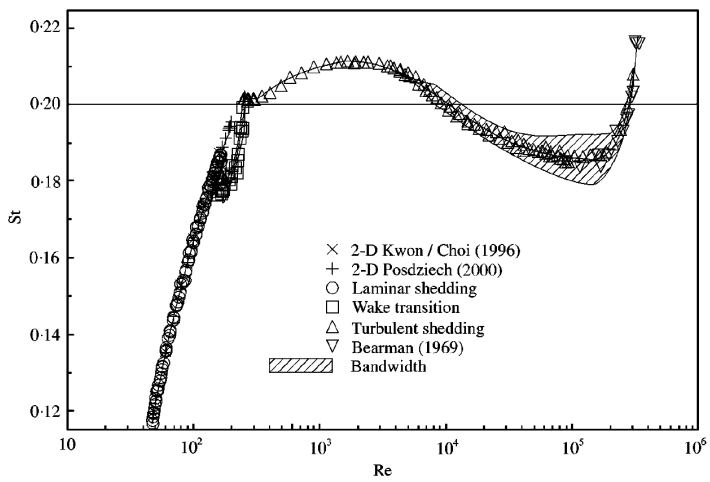

(a) Strouhals number, figure 1

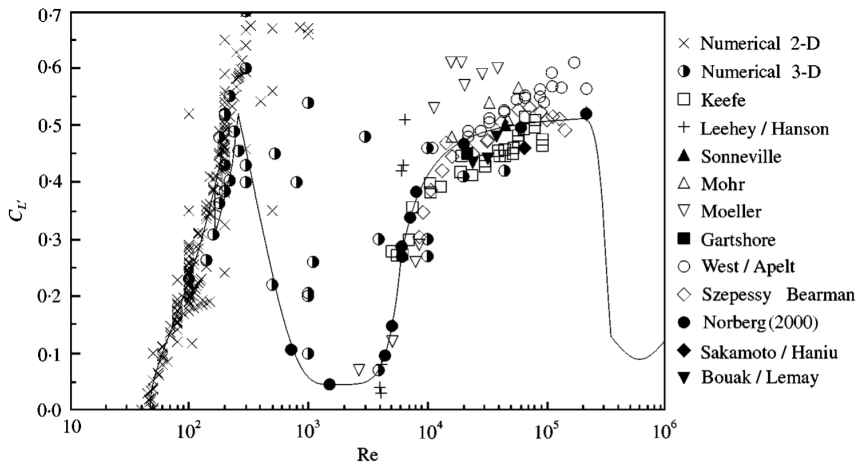

(b) $C_{L_{rms}}$, figure 2

Figure 8: Reference figures from Norberg (2001)

4 Reference Values

4.1 2D Simulations

The circular cylinder has been subject to numerous studies, both experimental and numerical. A classical experimental reference for Strouhals number is Roshko (1954). For $Re = 100$, he found $St \approx 0.167$. Similar values are given in the compilation graph by Norberg (2001), figure 8a. This compilation consists of two numerical and one experimental study. Next, the root mean square of the lift coefficient $C_{L_{rms}}$ is presented in figure 8b. 2D and 3D simulations suggest $C_{L_{rms}} \approx 0.23$ (C_{Lrms} is denoted by $C_{L'}$ in figure 8b). In Rajani et al. (2009), $C_{L_{rms}} \approx 0.18$. Additionally, Rajani et al. (2009) calculated the separation angle for $Re \in [0, 300]$, and this was compared to experimental values (cf. figure 9a). For $Re = 100$, the separation angle is found to be approximately 118°. Rajani presents drag coefficients in figure 9b, and for $Re = 100$, $C'_D \approx 1.40 \pm 0.02$. In B. N et al. (2017), $\theta_{reat} \approx 180°$.

4.2 3D Simulations

The references used for the 2D simulations also includes higher Reynolds number simulations/measurements. Figure 8a shows that $St \approx 0.20$ at $Re = 300$. Figure 7 in Rajani et al. (2009) illustrates that the flow is close to steady at $t = 75$ s and figures 7d and 7c gives $C'_D \approx 1.43$, $C'_L \approx 0.7$. In Sumer and Fredsøe (1997) the correlation length is given as $(2 - 3)D$.

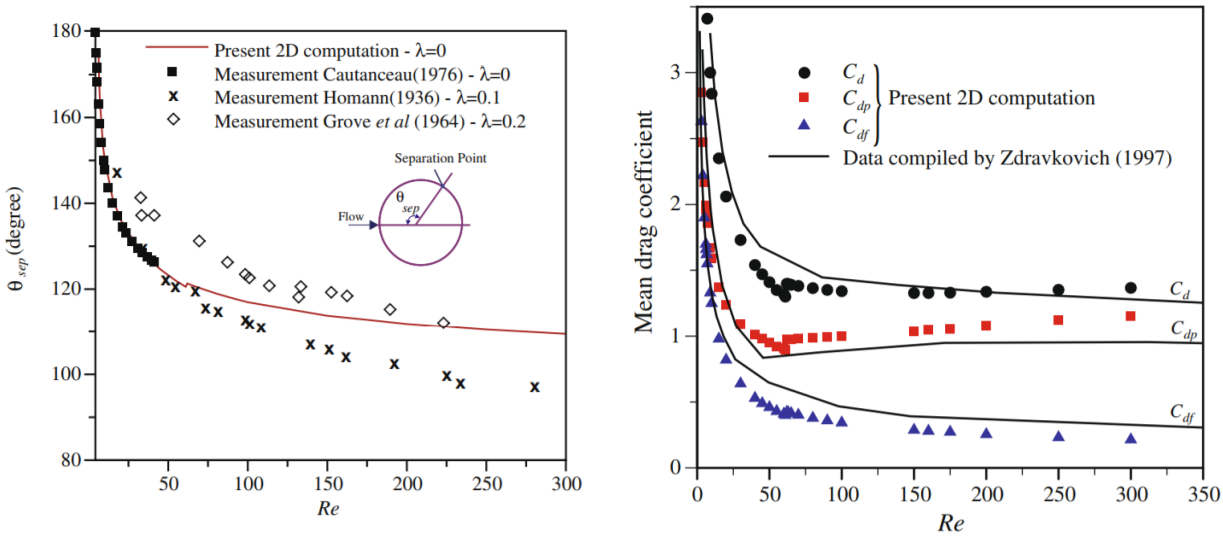

(a) Separation angle, figure 5a

(b) $C'_D - Re$ dependence, figure 6a

Figure 9: Reference figures from Rajani et al. (2009)

5 Results

5.1 2D Simulations

Task A

As described in the Methods section, after a first iteration the boundary layer thickness is estimated as $\delta \approx 0.3$. In figure 24 in the appendix, the boundary layer profiles for the different number of grid cells are presented: $N = 3, 6, 9, 12, 15$. Additionally, I concentrated cells radially to the wall in a geometric series with r = 1.05. I.e, the thicknesses will be given as t, tr, tr^2... As explained in the Discussion section, the grid density was set to $N = 12$, resulting in the boundary layer in figure 11a. This corresponds to a range of cell thicknesses in the boundary layer from approximately 0.003D to 0.005D. A close-up of the final boundary layer mesh is presented in figure 28b in the appendix.

Task B

In table 2, results for the primary variables for different domain sizes are displayed. The stream-wise velocity at the top boundary for the chosen domain size $\alpha = 6$ is given in figure 11b. In appendix 10.4, it is given figures for $\alpha = 2.5, 4, 6, 7$. Note, $a = \alpha D$.

Task C

In figure 26 in the appendix, the pressure contours at the critical locations discussed in section 4.1 are presented. The final mesh is given in figure 27 and consists of a total of 26 378 cells. In table 3, the primary variables are displayed for four different Courant numbers. The highest stable time step where found to be $\Delta t = 0.02$, corresponding to a maximum CFL number of $CFL = 1.04$. The time step was finally chosen to $\Delta t = 0.01$, corresponding to a miximum CFL number of $CFL = 0.51$.

Task D

As clarified in the discussion section, I have chosen the configuration presented in table 4. A simulation with this configuration provides primary variables as in table 5. In figure 13, the drag and lift coefficient time histories are presented.
The separation point varied with $\pm 2.6°$, and the mean separation was observed at $\theta_{sep} \approx 117.4°$. The reattachment point where found at $\theta_{reat} = 153° \pm 4.0°$. The localization of the separation and reattachment points are given in figure 10. The stagnation point were found to vary with an

amplitude of approximately 2.3° and was in phase with the primary flow structures. Furthermore, St_2 denotes the non-dimensionalized frequency of the second most important flow structure. This frequency was determined by investigating the FFT of the pressure at the numerical probe and is given as $St_2 \approx 2.25St$(cf. fig 12). The probe (a collection of 4 cells) was located at approximately $(x, y) = (3.2D, 1.3D)$. The secondary flow structures may be investigated by visualization of vorticity. In figure 14, a vorticity time series is presented to investigate the behaviour. Lastly, in figure 15, there is a combined vorticity-pressure contour plot.

α	C'_D	C'_L	St
2.5	1.69	0.646	0.214
4	1.476	0.354	0.226
6	1.416	0.332	0.172
7	1.416	0.332	0.171

Table 2: Primary variables task B

Δt	CFL$_{max}$	CFL$_{mean}$	C$'_D$	C$'_L$	St
0.02	1.04	0.090	1.419	0.343	0.192
0.01	0.51	0.046	1.419	0.339	0.168
0.005	0.26	0.023	1.417	0.340	0.164
0.003	0.19	0.014	1.419	0.352	0.131

Table 3: Primary variables and CFL task C

N	α	Δt
12	6	0.01

Table 4: Configuration in task D

C$'_D$	C$'_{D_d}$	C$'_{D_s}$	C$_{D_{rms}}$	C$'_L$	C$_{L_{rms}}$	St	St_2
1.419	0.014	1.405	1.406	0.339	0.237	0.168	0.378

Table 5: Results task D

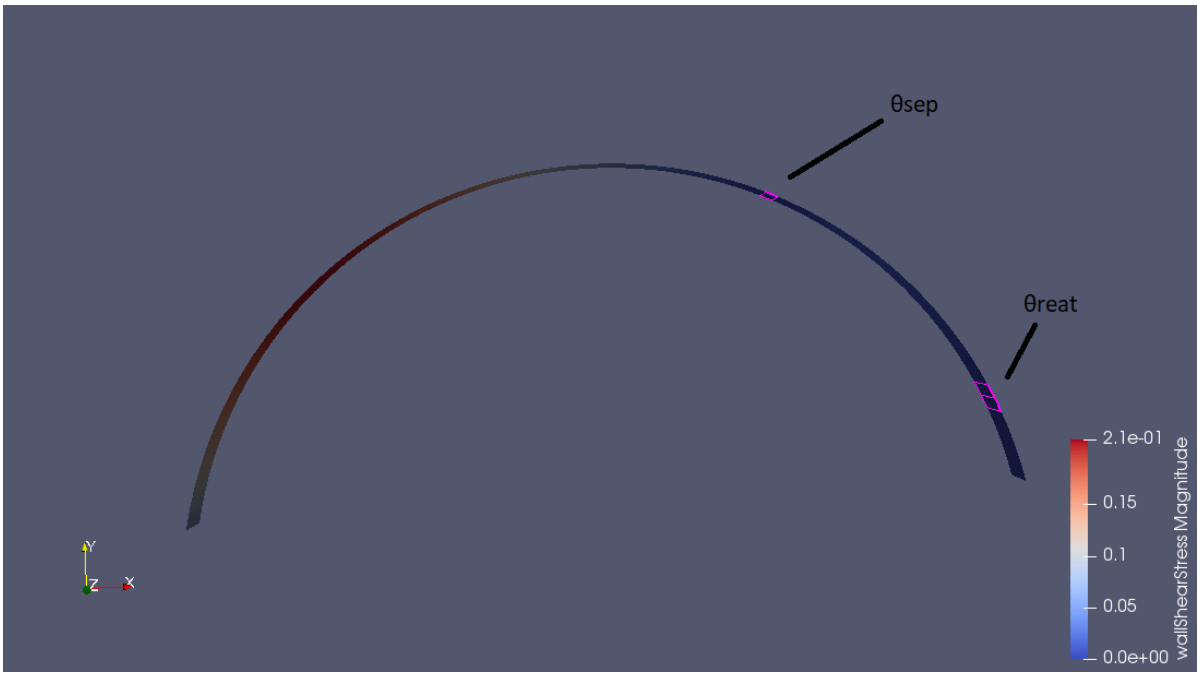

Figure 10: Separation and reattachment points

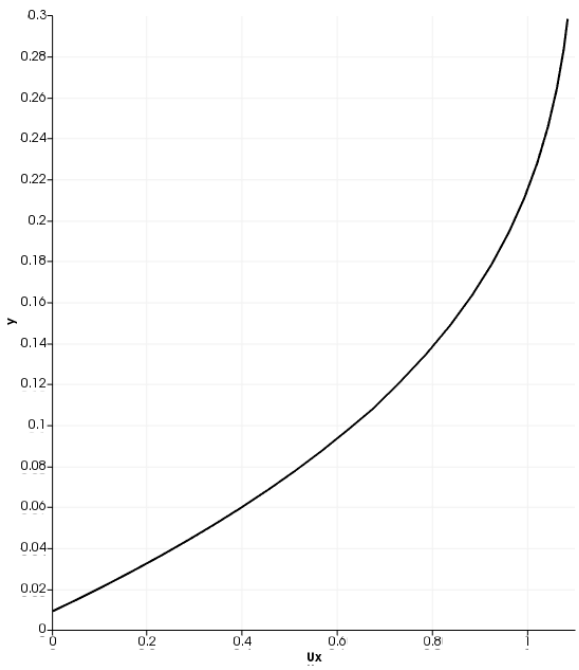

(a) Task A: $N = 12$

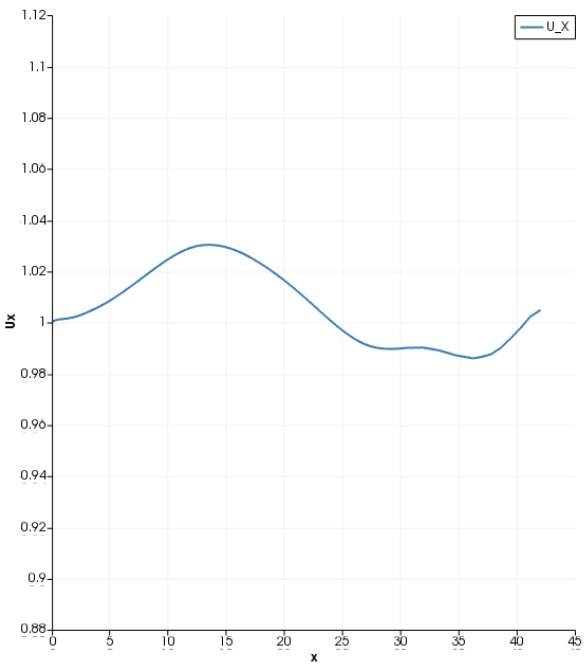

(b) Task B: $\alpha = 6$

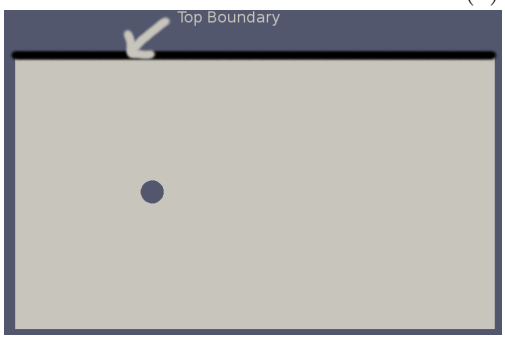

(c) Location of top boundary, $y = 12$

Figure 11: Final boundary layer profile, top streamwise velocity and top boundary location

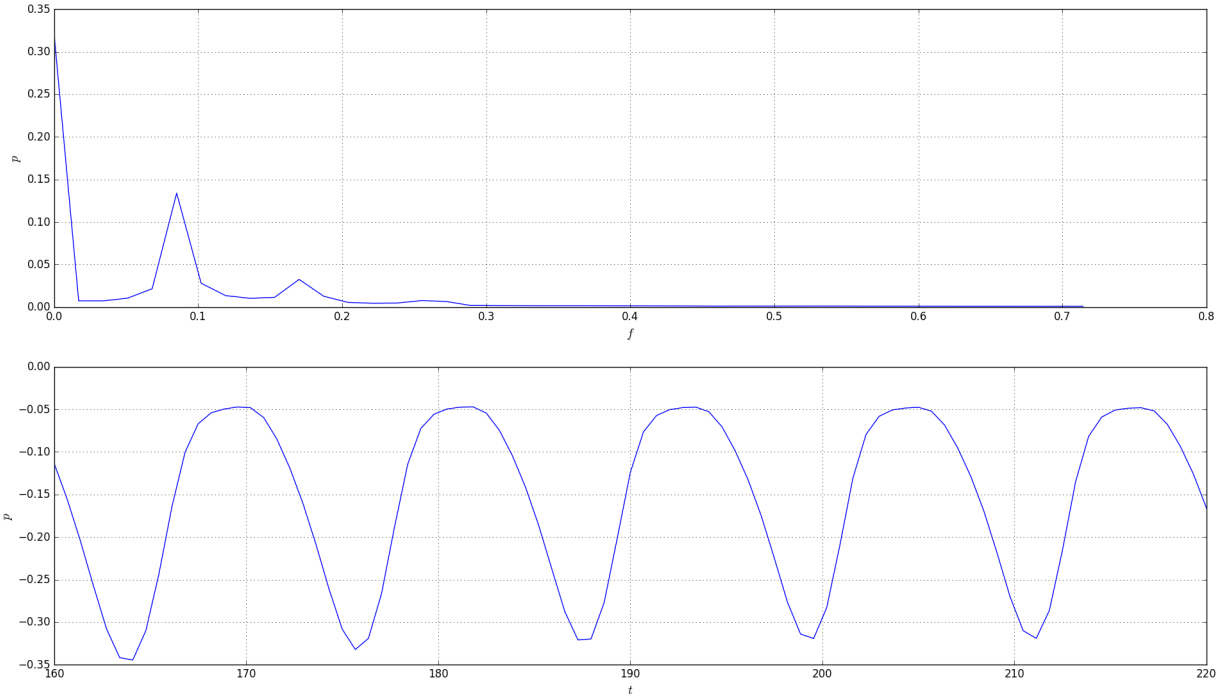

Figure 12: Pressure output task D

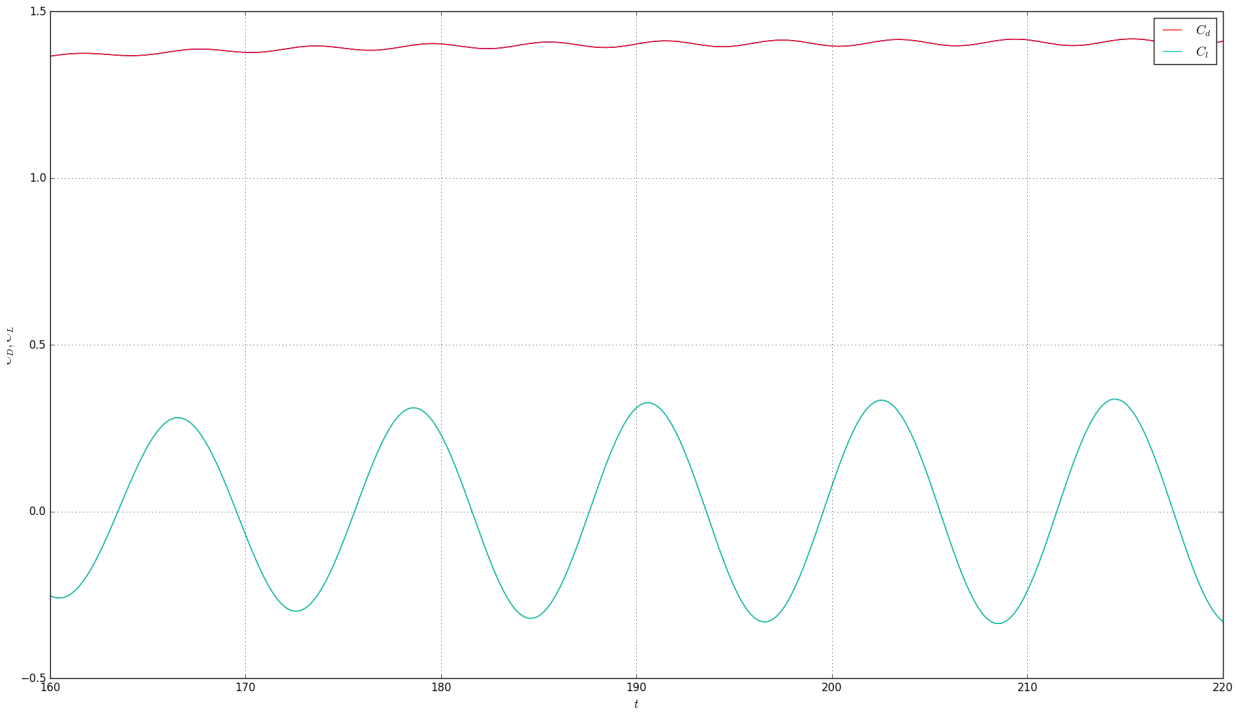

Figure 13: Drag and lift coefficients task D

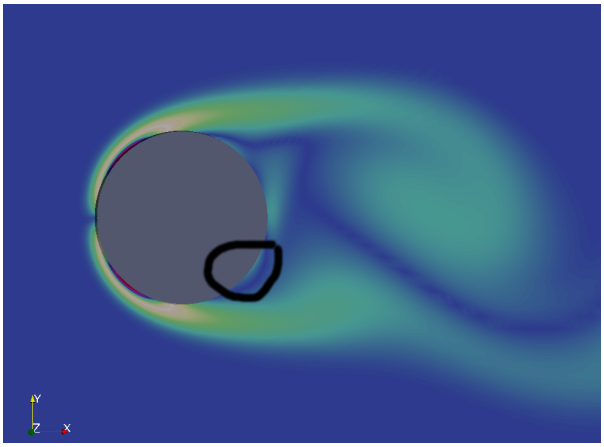

(a) $t = 208.6\ s$

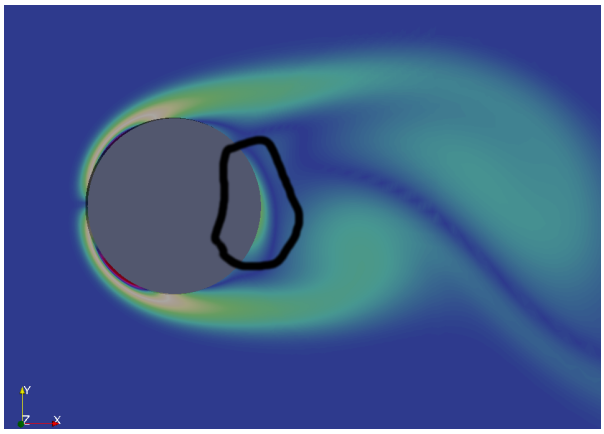

(b) $t = 210.0\ s$

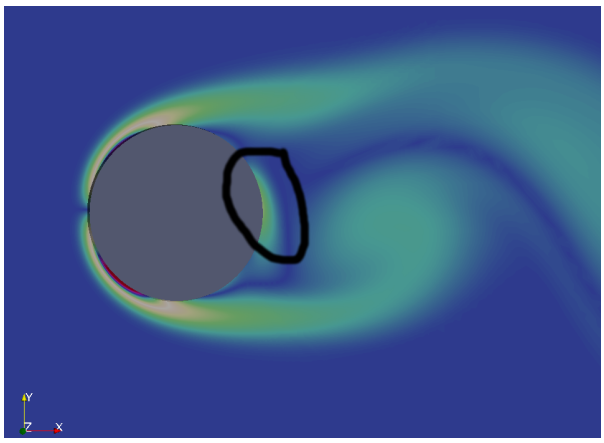

(c) $t = 211.4\ s$

Figure 14: Vorticity magnitude time series task D

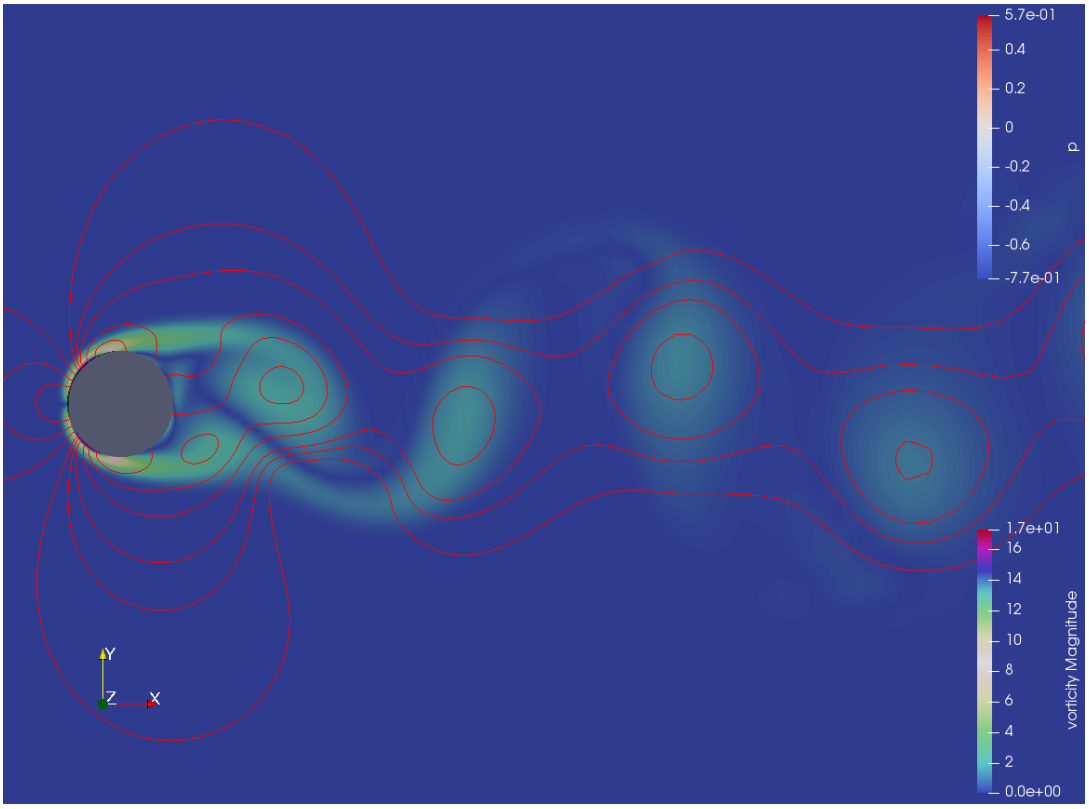

Figure 15: Vorticity-pressure plot task D

5.2 3D Simulations

Step 1

After a couple of iterations with $Re = 300$, I made a few changes to the grid. The boundary layer was kept unchanged, but the domain size was increased to $\alpha = 7$, which implies $a = 14$ (cf .figure 6). In appendix 10.7, figures of the boundary layer resolution, pressure contours, top- and outlet boundary streamwise velocities are presented.

Step 2

The mesh topology and a close-up of the mesh at the cylinder surface is given in figure 16. The mesh at the cylinder is concentrated towards the the center of the cylinder(z-direction), which is of most interest (due to the unphysical boundary conditions at the ends). The mesh passed OpenFOAMs checkMesh utility and the total number of cells equaled 769 440. After approximately $50s$, the flow turned three-dimensional. Especially the contour plots of λ_2 in figure 17 show the three-dimensional character of the flow. Thus, the initial mesh design was adequate to move to step 3.

Step 3

Figures 19a-d show the complex 3D structures in the wake. Here contours of λ_2 are used to depict the coherent flow structures in a time series. A top-down picture of the coherent structures is given in figure 18. The spatial vortex evolution is given in figure 19, where x_s is the distance downstream of the cylinder where the visualization was clipped/sliced. Figure 20a-b illustrates the $p - \lambda_2$ interdependence and figure 20c presents the z-averaged pressure signal in the time and frequency domain. The primary variables are given in table 6. The increase in the CPU metric q from the 2D simulations was a factor of 80.

St	C'_D	C'_L
0.38	1.29	0.31

Table 6: Primary variables 3D simulation

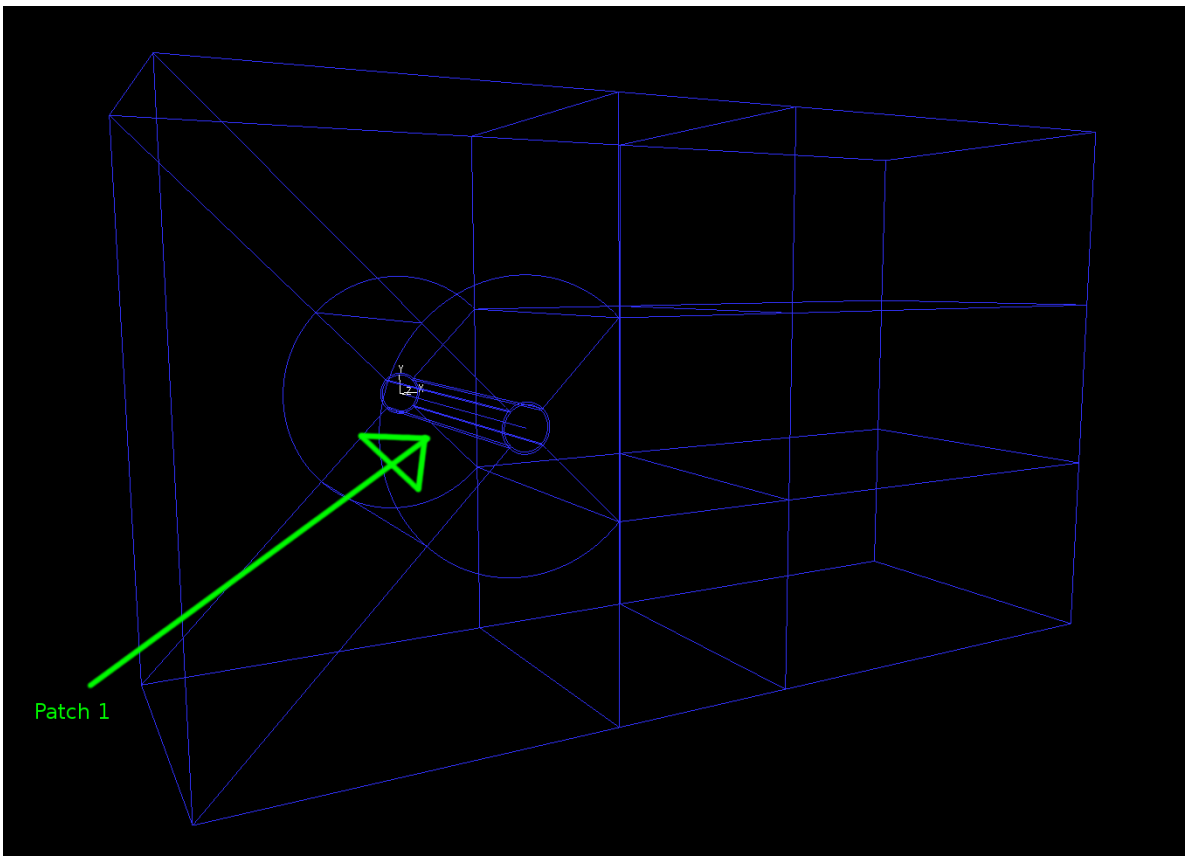

(a) Mesh topology 3D

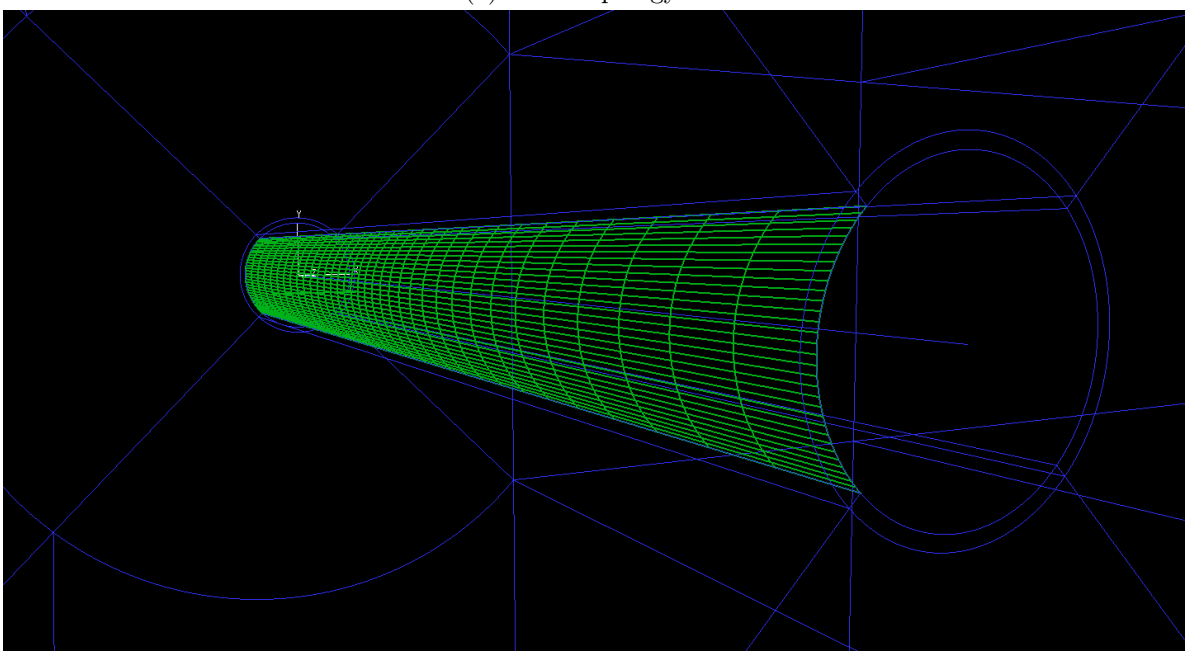

(b) Boundary layer resolution patch 1

Figure 16: Mesh after step 2

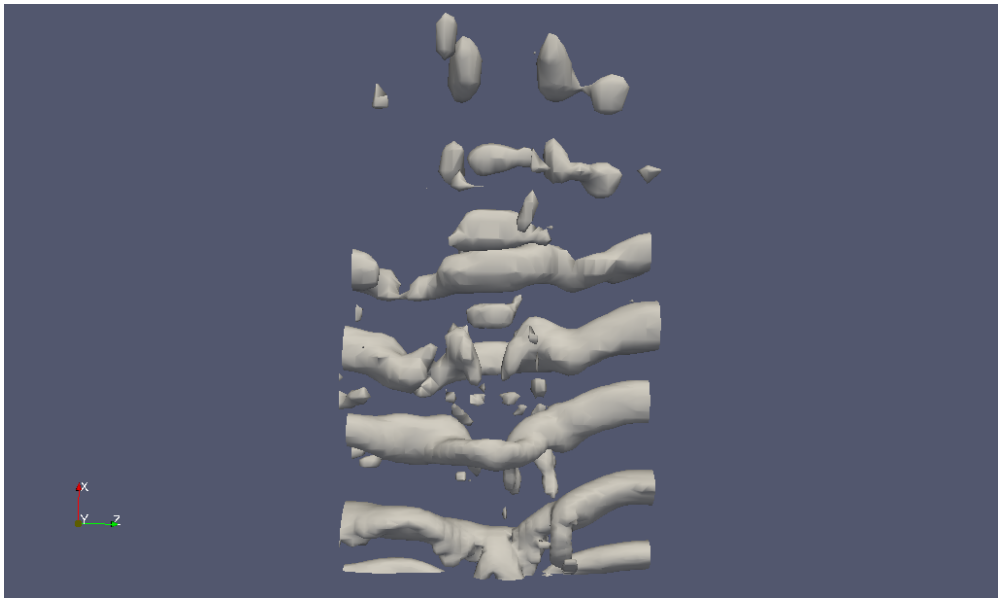

Figure 18: Top-down view of λ_2

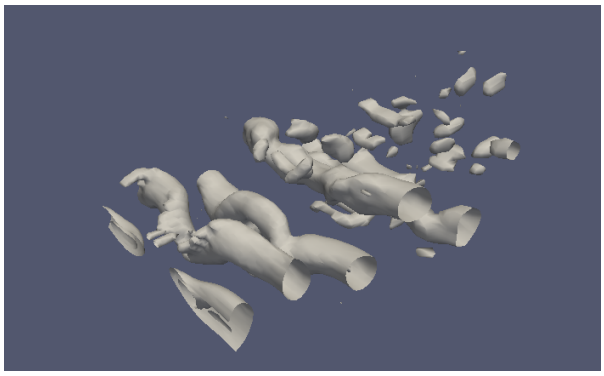

(a) $t = 68\ s$

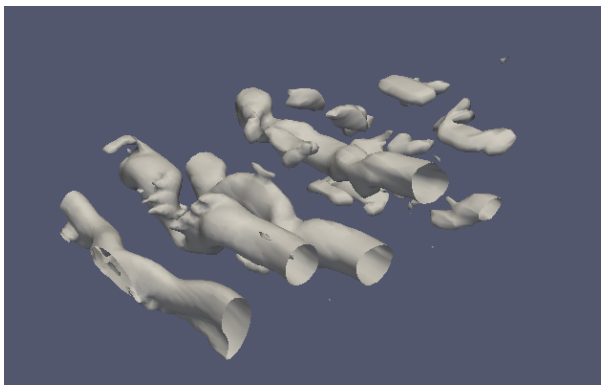

(b) $t = 68.8\ s$

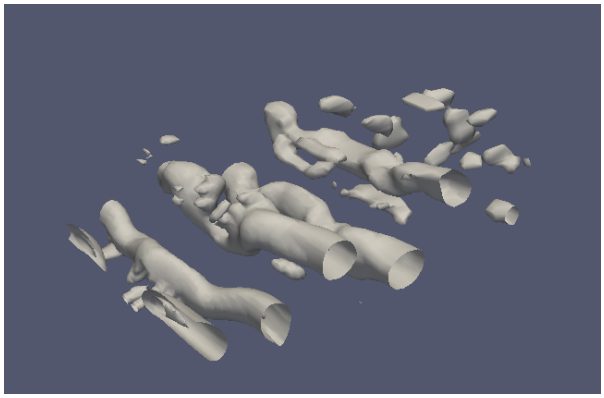

(c) $t = 69.6\ s$

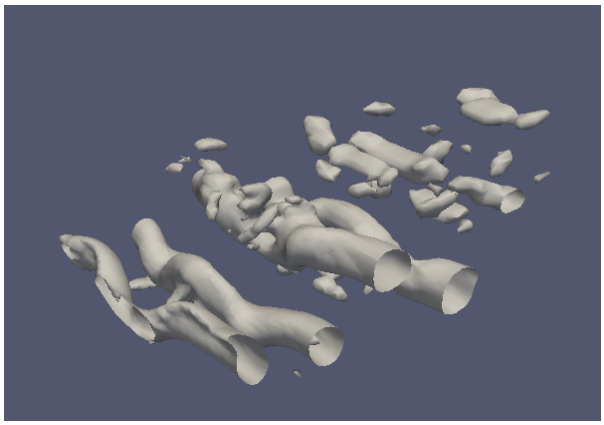

(d) $t = 70.4\ s$

Figure 17: Temporal evolution of flow structures, λ_2 method

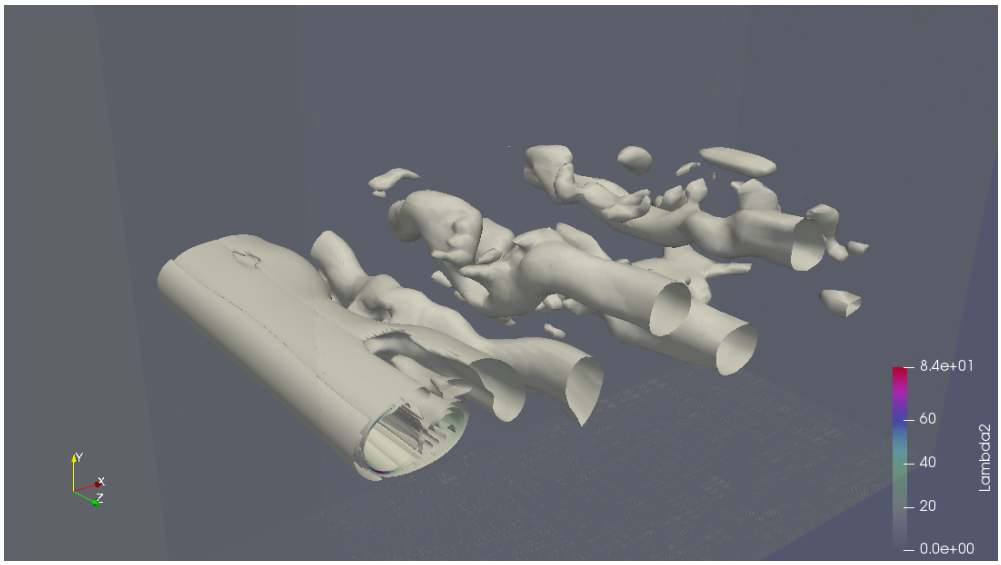

(a) $x_s = -D$

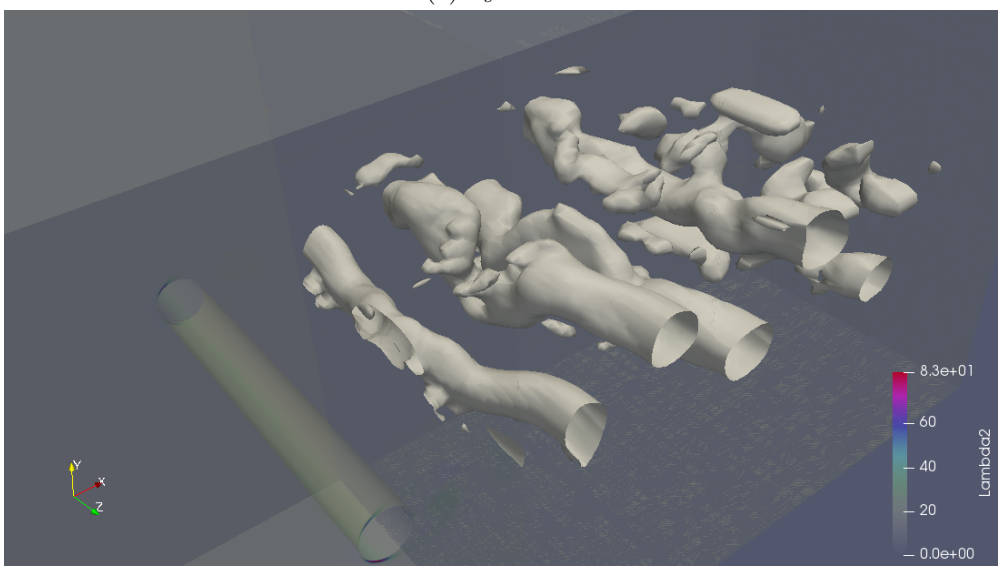

(b) $x_s = D$

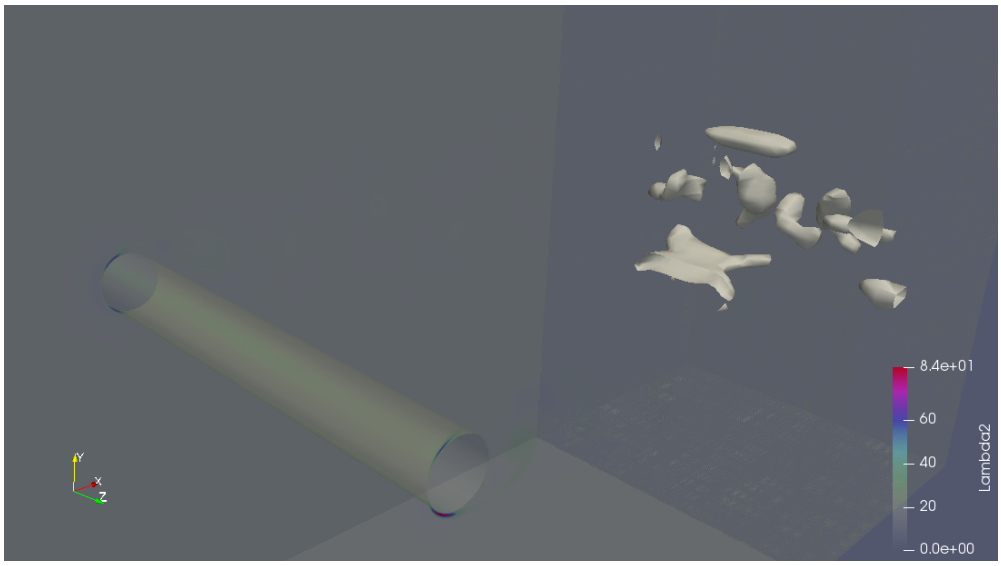

(c) $x_s = 5D$

Figure 19: Spatial evolution of flow structures

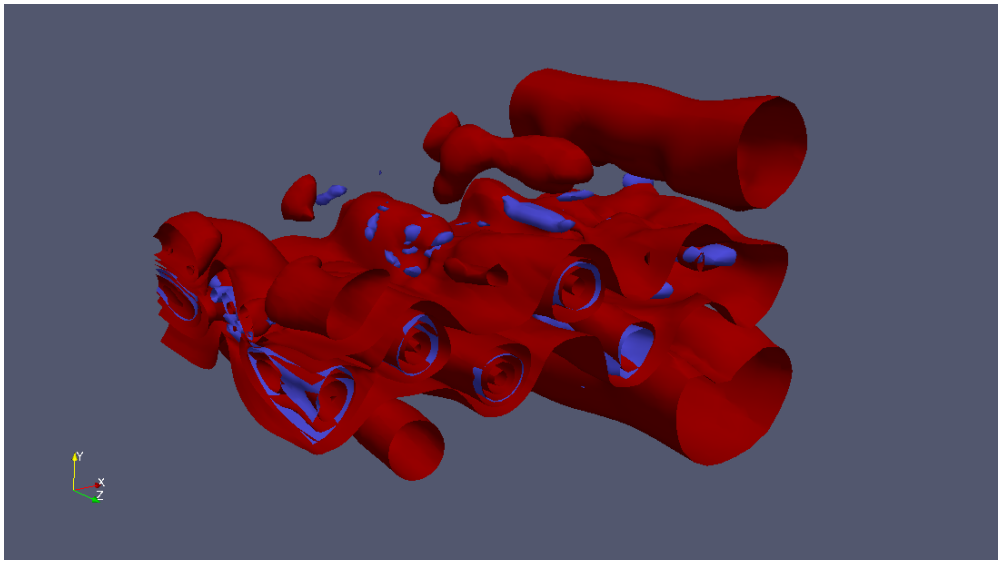

(a) Pressure(blue) & λ_2(red) contours

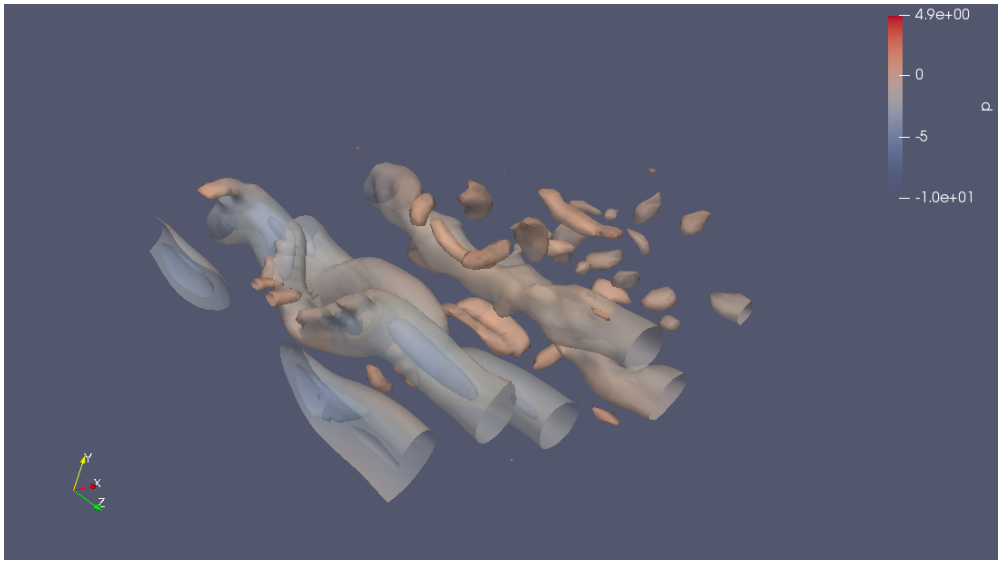

(b) Pressure coloured λ_2 contours

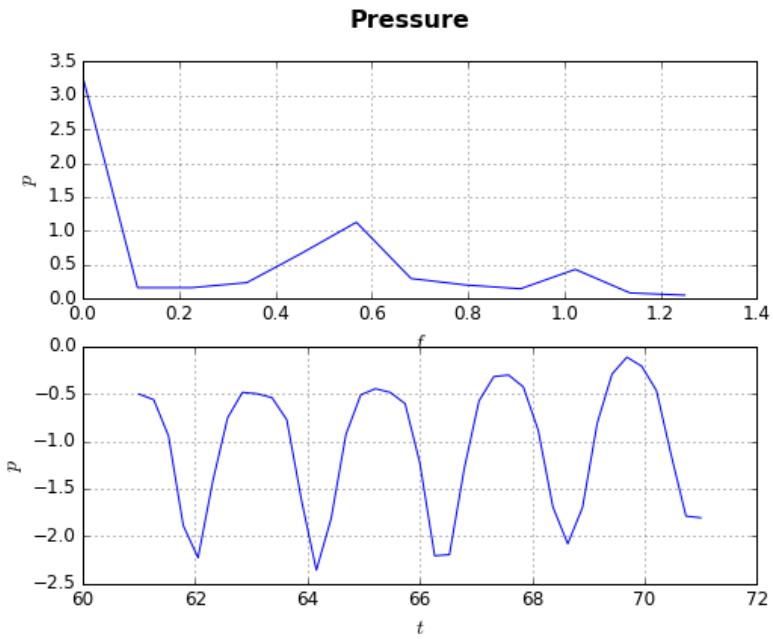

(c) Z-averaged pressure signal in time and frequency domain

Figure 20: Pressure - λ_2 interdependence

6 Discussion

6.1 2D Simulations

Task A

Figure 24 shows that the boundary layer is clearly unsmooth for $N = 3$ and $N = 6$, and that these profiles differ significantly. From $N = 6$ to $N = 9$, there is a relatively small change in the profile. However, the resolution is still somewhat unsmooth at $N = 9$. At $N = 12$, the grid is smooth and there is little change from $N = 9$. Based on visual inspection, the profile at $N = 15$ is identical to the profile at $N = 12$. Hence, I decide to use $N = 12$ as the boundary resolution as the profile is smooth and seems to have converged. I expect that using $N = 9$ would have produced similar results in task B,C and D. A slightly more sophisticated convergence study could investigate the development in 2-norm of the boundary layer profile. When the change in 2-norm from one resolution to the next is less than some tolerance, the boundary layer could be considered as converged. I.e.,

$$\frac{L_2(U^{i+1}) - L_2(U^i)}{L_2(U^i)} < tol \tag{33}$$

Task B

The results in table 2 and figure 25 suggest that both $\alpha = 6$ and $\alpha = 7$ are appropriate domain sizes. There are significant changes in C'_D, C'_L from domain size 2.5 to 4 and 4 to 6. The change in the primary variables from 6 to 7 is just a slight change in St. That is also the case when looking at the x-velocity at the top boundary. There is convergence for the x-velocity with variations of roughly 3% from the free stream velocity. Conclusively, with small changes from $\alpha = 6$ to $\alpha = 7$, I consider that the solution has converged with respect to domain size with $\alpha = 6$. As aforementioned, this convergence study, using the primary variables, is far from rigorous but sufficient for this study's objectives. In line with the proposed extension in Task A, the development in 2-norm of the streamwise velocity could have been investigated. However, the potential flow solution at the top boundary do change with α. Hence, the tolerance criteria would have needed to take this effect into account. A natural starting point for devising this criteria would be the potential flow solution. Alternatively, this study could be used to derive new boundary conditions on the top and bottom boundary of a non-zero gradient type. To verify this boundary condition, the smoothness of the flow close to the boundaries would have been investigated.

Task C

The pressure contours in figure 26b and 26c indicate that the pressure is continuous at the boundary layer. In figure 26a, one may observe minor discontinuities in the right boundary of the C(intersection zone 2 and 3). The grid was refined in these areas, but this problem is inherent in the C-mesh topology. The effect of these discontinuities is hard to evaluate, but could be further assessed/prevented by a finer contour resolution and a resulting mesh refinement. Regarding the time step, the first simulation with $\Delta t = 0.02$, may be disregarded due to discretization errors. In the solution of a nearly unstable flow, instabilities may propagate in some parts of the flow, while they later are convected and damped elsewhere. With a time step decreasing below $0.01s$, the primary variables seem to diverge rather than converge. Due to this behaviour, $\Delta t = 0.01$ was determined as the final time step. One possible explanation is accumulation of round off-errors. This computation is relatively short in terms of time steps, so I find this explanation unlikely. Another explanation is possible oscillations due to the FVM method used in the spatial discretization (Jasak, 2015). One way to investigate this would be using an alternative method, e.g. the 1st order upwind scheme. This scheme introduces numerical viscosity and hence avoids the oscillations. However, this method is 1st order accurate so a finer grid would have been needed. An alternative 2nd order method could also be utilized, but then introduced other numerical characteristics. In essence, it is not straightforward to compare the performance of different FVM methods. Thus, a further investigation of the temporal discretization error by use of an alternative FVM methods was not pursued.

Task D

The obtained primary variables are in good accordance with experimental and numerical references. C'_D is within the range specified in Rajani et al. (2009). Similarly, $C_{L_{rms}}$ is in accordance with Norberg (2001). In figure 13, C'_D and C'_L behaves periodically with fv and $2fv$ (cf. section 2.3). However, figure 12 shows that the flow is not steady until 180s. The Strouhal number is close to that specified in Roshko (1954). This good correspondence strongly indicates that the flow is correctly resolved. This is also the case with the separation point with regard to Rajani et al. (2009). As the primary variables are accurate, this is to be suspected since the separation point is determining for the vortex dynamics. The separation point is again determined by a proper resolution of the boundary layer. However, due to the inaccuracy in the literature review, it is hard to tell how accurate the results are. As most graphs in the literature review only indicate results, I can only estimate values. My results are within the area of read off error, which gives an indication of the accuracy of this study (I.e., within a few percents of the primary variables). With such a rough estimate of the correct result, it is not possible to consider the magnitude of the discretization errors. In a more comprehensive study, first a literature review would have provided accurate values of the primary variables. Then, following the present work, a more thorough convergence study could have been performed(Wang et al., 2008). Given these results, an assessment of the accuracy of the numerical method could have been performed. In this simulation, there are no modelling errors, making such an assessment relatively straightforward. As a sidenote, for instance in a RANS simulation (cf. section 2.4), the above procedure could be used to estimate the turbulence modelling errors. I.e., by minimizing the discretization errors by a proper convergence study, the discretization errors would be negligible compared to modelling errors. Then, somewhat simplified, the quality of a given turbulence model could be assessed.
Regarding secondary flow futures, reattachment plays an important role in the vortex dynamics. The identified reattachment angle deviates significantly from B. N et al. (2017) ($\approx 25°$). This may indicate that the boundary layer and wake just downstream is not sufficiently resolved to predict this phenomena accurately. In figure 14, the temporal evolution of one vortex of interest(black encircling) is tracked. A discussion on its time evolution is placed in the appendix, as it is rather speculative. Figure 15 confirms that vortices have pressure minimums at their centre. Hence, for frequency information regarding vortex dynamics, it is equivalent to perform a FFT of the vorticity or the pressure (cf. section 2.3).

6.2 3D Simulations

Step 1

As the flow is 3D, the 2D simulations do not portray the flow correctly. Nevertheless, I assume they have some value in early mesh design. From a computational point of view, a good 2D mesh reduces the amount of verification needed for the 3D mesh. Figure 29a shows a smooth boundary layer, indicating it is correctly resolved. The boundary layer thickness at $Re = 300$ is given as $\delta \approx 0.19$. See appendix 10.1 for a discussion on the development of the boundary layer thickness. Further, the pressure contours are continuous throughout the domain except at the critical C-Mesh locations. Following the same argumentation as in the 2D case, I assume this effect to be negligible. Figures 29c-d, show that the vortex shedding is more dramatic for $Re = 300$ than for $Re = 100$; the vortices are shed such that they create a wider wake than in 2D. As the flow is more energetic, this seems reasonable. Given figure 29c, one may argue that the domain size should be increased further. Even though the velocities considerably exceed the free stream velocity, this occur far downstream. Hence, I assume the boundary conditions at the top and bottom boundary will not effect the solution just downstream of the cylinder significantly. As discussed for the 2D simulations, new non-zero gradient boundary conditions could be derived to avoid this issue.

Step 2

Given the visual check and acceptance of the checkMesh utility, the mesh should be usable for simulations. The results in figures 17-20, show that the mesh is able to capture three-dimensional

effects. However, the mesh is very coarse in the z-direction (35 cells) and the boundary conditions at the front and back boundaries have a significant effect on the three-dimensionality of the flow. The zeroGradient condition implies no z-variations and thus 2D flow close to the front and back boundaries. This can be seen in figures 17-20. Thus, the length of $8D$ is sufficient to produce 3D effects given these boundary conditions, but the flow is greatly effected. This flow is then merely useful for investigation of 3D separation in general, and not to predict the primary variables for a 3D cylinder at $Re = 300$. To do so, the numerical grid would have needed to be extended in z-direction until the zeroGradient condition had been satisfied(checked with the similar procedure as in task B for the 2D simulations). Another possible step to improve the grid would have been to perform a convergence study based on the grid resolution in z-direction. This is of interest as small and large scale 3D effects are of interest. Then, the development in primary variables could have been used as convergence criteria. However, this would have required multiple costly 3D simulations and was therefore not pursued.

Step 3

Figure 17 shows that at the front and back boundaries the flow behaves two-dimensionally in the initial wake. However, further downstream the 3D vortex dynamics results in a gradual disintegration of the structures. I assume this to be caused by diffusive effects, where vorticity is diffused and counteracting vortices cancels. Furthermore, the middle part of the flow structures (in z-direction) attract each other, such that the upper structures (moving at y>0) is attracted downwards to the lower structures (moving at y<0) and vice versa. As the structures move downstream, they interact and gradually cancels each other and dissipates. It first occurs in the middle, where the structures are not restricted by the zeroGradient boundary condition, and then gradually moves towards the front and back boundaries. The disintegration can clearly be seen in figure 19c, where 5D downstream the structures have almost completely disintegrated. Due to the boundary conditions in z-direction, the flow is forced towards symmetry about the x-y plane. However, figure 18 shows that the flow is asymmetric around this plane. This indicates that the actual external flow around a 3D circular cylinder is asymmetric in the x-y plane, as this is less constrained than this artificial simulation. Asymmetry is important, as it implies a moment resultant M_y.
Figures 20a-b show that there are pressure minimums inside coherent structures. Figure 20b shows that stronger the vortex the lower the pressure minimum. This is in correspondence with Jeong and Hussain (2006). Furthermore, the pressure signal in 20c indicates that the flow is not yet statistically steady. As mentioned in section 16, the flow is close to steady at $t = 75s$. Given the purpose of this study, this is considered as an insignificant effect. Thus, the primary variables are not completely correct for this flow configuration.
This effect is assumed to be small compared to the effect of the artificial boundary conditions, which presumably cause the large discrepancies from the reference values in 4.2. First, the Strouhals number is off by 90%, indicating that the vortex dynamics do not resemble the real flow. This effect is most obvious on C'_L with a deviation of 66%. This is to be expected as lift is directly related to the vortex dynamics. The difference in C_D is smaller, 10%, and this is because the skin friction constitutes the majority of the drag (for $Re = 100$ it was 99% of the total)(cf. 9b) and is not that influenced by the artificial boundary conditions. However, I assume the form drag is greatly effected, and this causes the significant deviation. The above primary variables are all calulated based on the flow along the entire cylinder length. More reasonable results are to be expected if only forces and vortex shedding had been investigated at the mid-part of the cylinder. Lastly, Sumer and Fredsøe (1997) states that the correlation length at $Re = 300$ is $2D - 3D$. If one defines the middle part of the sheddings as distinct structures, they have a length of approximately $2D - 3D$. The lambda2 method do not make this distinction, but such clear distinctions of different vortices is a known problem with this method. However, the results indicate that they may evolve into separate structures in a real flow, where two-dimensionality is not imposed. The development in CPU time from 2D to 3D, is discussed in appendix 10.1.

7 Turbulence Modelling for Flows around Bluff Bodies

Ship resistance is an inherently viscous problem. As potential flow theory is unable to predict skin friction and experimental methods are costly, viscous simulations have a great potential to estimate ship resistance efficiently. Thus, the first comprehensive efforts towards bringing CFD to the marine field was in numerical ship hydrodynamics. In 1980, the first workshop on numerical ship hydrodynamics was arranged in Gothenburg, and has since been arranged every five years. As simulation techniques and turbulence models have become more sophisticated, the prediction of flow separation has drastically improved. In turn, this results in improved predictions of form drag and wake dynamics. With these capabilities, CFD has become a relevant tool in predicting the flow around bluff bodies. This is of particular interest in the offshore industry, where bluff bodies are common and there is a pressing need to accurately predict vortex induced vibrations.

7.1 The Workshop on Numerical Ship Hydrodynamics 1980-2010

When the first workshop on numerical ship hydrodynamics was held in 1980, the purpose was to assess the state of the art in numerical hydrodynamics and to provide guidelines for future developments (Larsson et al., 2014). In the first workshop, all methods were of the boundary layer type (cf. section 2.5). In 1990, most methods were RANS-based with simple isotropic turbulence models (two-equation and mixing length). This resulted in huge improvements in the calculations of the stern flow. During the 1994 and 2000 workshops, free-surface modelling and more formal verification and validation procedures were included. In the 2010 workshop, three standardized hulls were used to assess resistance, local flow field at the propeller plane, self-propulsion and sea-keeping. I will assess the two former ones, which are relevant for turbulence modelling of bluff bodies.

For the resistance predictions, the mean standard deviation of the error between the computed and measured value(D) for all test cases was 2.1%D. This indicates that the skin friction and form drag are both reasonably predicted. In these simulations, it was not seen any improvements in predictions with turbulence models more sophisticated than the two-equation models. These rather simple and extensively tested models provided the best results. However, in this case, the number of simulations with advanced turbulence models was limited. In conclusion, two-equation models with low Reynolds number wall treatments were seen to be sufficiently advanced to predict the resistance quite accurately.

More relevant for bluff body turbulence modelling is the results of the local flow field in the ship stern (Re was in the range $10^6 - 10^7$). Due to the formal grid verification procedures at the workshop, Larsson et al. (2014) note that the dominating part of the error is due to turbulence modelling (cf. section 2.8). Cf. table 3.1 in Larsson et al. (2014) for the applied turbulence models in one of the test cases. Note that for all 12 models except one, a special low Re near wall treatment is used. I.e., conventional wall functions are unsuitable to predict the flow separation occurring in the ship stern (cf. section 2.5). The results show that in order to accurately predict the local flow field, an anisotropic turbulence model as RSM, EASRM or DES is needed. This is in correspondence with the discussion in section 2.6. Larsson et al. (2014) highlight that EASRM produces the best results considering robustness and computational cost. Lastly, it is noted that there is still considerable room for improvements in RSM, DES and EASRM models. Particularly, the use of DES, and its modification DDES, were at the time considered as immature for marine applications.
Conclusively, in 2010 turbulence modelling of the ship stern, which may be considered as a bluff body, was relatively accurately predicted by anisotropic turbulence models. Most turbulence models in use were RANS-based, but also DES was starting to become a viable option. However, it is important to note that all these simulations are in model scale. Besides turbulence modelling, systematic verification and validation procedures were formalized. The above provides an indication of the state-of-the-art of marine CFD in 2010.

7.2 Turbulence Modelling of Bluff Bodies

In this main part of the review, I will present research efforts focusing on validation of turbulence modelling of bluff bodies at high Reynolds numbers. The papers are presented in increasing degree of model complexity/computational cost. Most of the studies include multiple models, so this chronology is only schematic. The included models range from two-equation RANS models to LES, but the emphasis is on anisotropic RANS and hybrid RANS/LES models. I.e., I consider these models to reasonably compromise between accuracy and computational cost relative to engineering purposes. This consideration is confirmed by the review. The studies included in this review range from 2014-2017, where a majority were published in 2016-2017.

Eça et al. (2017) validated the RANS models SST $k-\omega$ and Spalart & Allmaras for flow around a squared column with rounded corners with $Re = 10^5, 10^6, 10^7$. The results were validated against experimental data, and the simulations were performed with ReFRESCO. It is noted that for even the simple assumption of two-dimensional flow, the level of grid refinement and iterative convergence criteria required to obtain acceptable numerical uncertainties are more demanding than usually observed in the literature; with half a million cells, numerical uncertainties of selected flow quantities (C_{D_s}, St etc.) are not below 5 %. Further, only the SST $k-\omega$ model at $Re = 10^5$ is able to predict zero lift statistically. A possible explanation of their behaviour is that theses models were developed for statistically steady problems, making them unsuited for the complex separating flows around the squared column. As the applied models struggle to predict the simplified 2D flow, the authors suggest that the models are not sophisticated enough to reproduce the actual 3D flow.

In van Raemdonck et al. (2016), RANS simulations of a generic truck model is validated against experimental data. The two models in use were SST $k-\omega$ and realizable $k-\epsilon$ (a modified $k-\epsilon$ model), and the commercial software package FLUENT was used. The authors note good correspondence in the attached boundary layer flow seen in the front, at the sides and at the top of the truck. Boundary layer parameters as boundary layer thickness and momentum thickness are in good correspondence with experimental data. However, the wake structure deviate significantly from the experimental values. In figure 21, the rear pressure distributions of the experimental and numerical results are presented. The authors suggest the discrepancy is because RANS forces steadiness on the flow, while it is highly unsteady in the wake. I.e., in equation (15), $T \not\ll T2$. Hence, two equation models do not seem to adequately model highly separating flows, but do predict attached boundary layers quite well. The authors suggest the models may be used in the preliminary design phase to get an estimate of mean force coefficients, but not to optimize rear truck design.

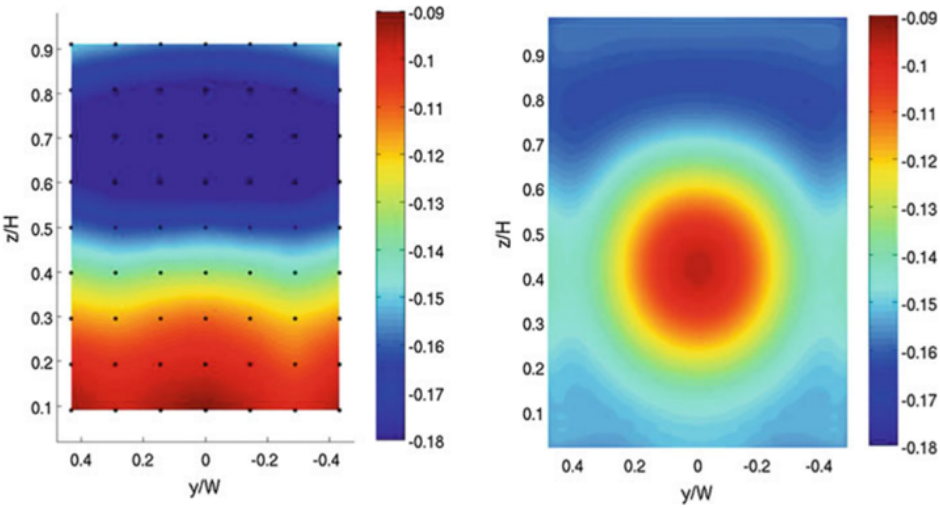

(a) PIV - Rear pressure

(b) RANS - Rear pressure

Figure 21: Rear pressure distributions in van Raemdonck et al. (2016))

A comprehensive validation study of different RANS models was performed in Pereira et al. (2017). 11 eddy viscosity based models and 3 EARSM models were validated by performing resistance and local flow field simulations of a KVLCC2 tanker (one of the test cases in the workshop on numerical ship hydrodynamics). The free-surface was neglected and none of the models used wall-functions, but rather a special low Re near wall treatment. The convergence properties of the different models were assessed with the ASME V&V20 procedure. The results were qualitatively in line with the 2010 Gothenburg workshop on numerical hydrodynamics. The eddy-viscosity based models accurately predict the total resistance and show good convergence properties. EARSM produce worse predictions of the total resistance, but provides better estimates of the local flow at the ship stern (cf. figure 11 and 12 in Pereira et al. (2017)).

Contrary to standard two-equation models, DES and SAS formulations are still under development. In Moussaed et al. (2014) a new DES formulation is tested on a circular cylinder at $Re = 1.4 * 10^5$. This formulation includes an automatic switch between RANS and LES by use of a blending function. This switch is meant to alleviate the earlier a priori specification of RANS and LES regions, making the DES pre-processing less laborious and error-prone. The predicted main flow parameters are generally in good correspondence to reference values, but the authors reckon that further development efforts on the RANS-LES switch are needed.

In Wu et al. (2016), the vortex-induced motion of a square cylinder is studied. The simulations were performed with OpenFOAM's pimpleDy solver, which allows mesh movement in one direction. The flow was simulated at $1500 \leqslant Re \leqslant 14000$ with the three models DDES(Delayed DES), DES-SST $k-\omega$ and DES-SST $k-\omega$. The movement of the square cylinder was validated against experiments and showed decent agreement with the DES-SST $k-\omega$ and DDES models and very good agreement for SAS-SST $k-\omega$(cf. table 3 in Wu et al. (2016)). Thus, only the SAS-SST $k-\omega$ was used in the subsequent simulations. As the cylinder length was varied, the simulations produced good quantitative results and the correct wake modes were observed.

Zheng et al. (2016) conducted a validation study of the SAS and DES SST $k-\omega$, where the emphasis was particularly on the former model. The validation test cases was a circular cylinder and a NACA0021 airfoil at angle of attack 60° at $Re = 1.4 * 10^5$. Both of the test cases are characterized by massive flow separation. Force coefficients are well predicted by both models, but SAS was the more accurate(cf. table 2 (Zheng et al., 2016)). For SAS, mean flow properties are accurately predicted, while second order turbulent statistics only show reasonable correspondance. Allover, both models perform well, but SAS do in general achieve better accuracy than the DES SST $k-\omega$ model for these validation cases

.

A comprehensive study of DES and LES was conducted by Serre et al. (2013) on the Ahmed body for $Re = 768\ 000$. Three different LES models and the DES SST $k-\omega$ model were studied. The level of detail in these simulations are illustrated in figure 22. All models were shown to produce results with good overall agreement with experiments, but significant deviations were observed for all models. E.g., a LES model with a near wall treatment did not predict the onset of separation correctly. Another high-order LES model, predicted incorrectly a confined recirculation zone at the front of the body, resulting in a dramatic overestimation of the drag coefficient (44%). The authors reckon LES simulations to be costly, but assess LES and DES to be the right level of turbulence modelling to accurately predict highly separating flows at high Reynolds number. They argue that further improvements of LES and DES algorithms are needed to improve accuracy and to reduce the computational cost. The results show that DES is a viable option to LES, but further algorithmic developments are needed.

In Vaz et al. (2017), a comprehensive validation study of different turbulence models are conducted for the flow cases: circular cylinder at $Re = 3\ 900$, 140 000 and a rounded square prism at $Re = 100\ 000$ at incidence angles 0° and 45°. The models under investigation were: SST $k-\omega$, EARSM, DDES, XLES (similar to DDES) and PANS (hybrid between RANS and DNS). The

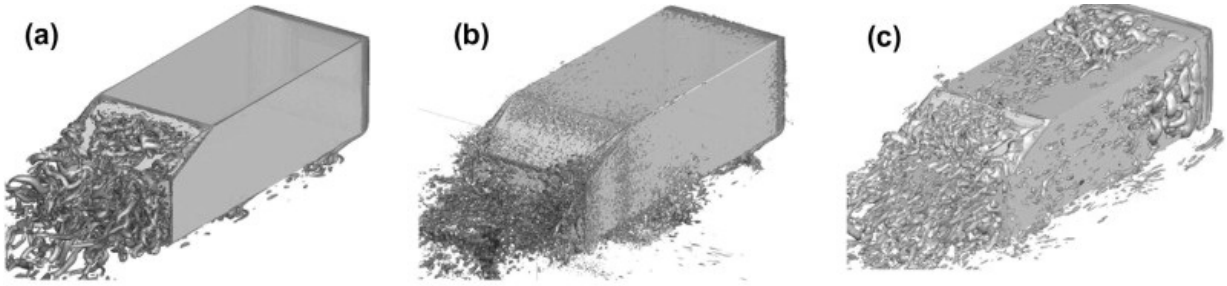

Figure 22: Vortex structures visualized by iso-surfaces(Q-criterion, Q = 60): (a) DES-SST, (b) LES-NWR, (c) LES-SVV (Figure 6 in Serre et al. (2013))

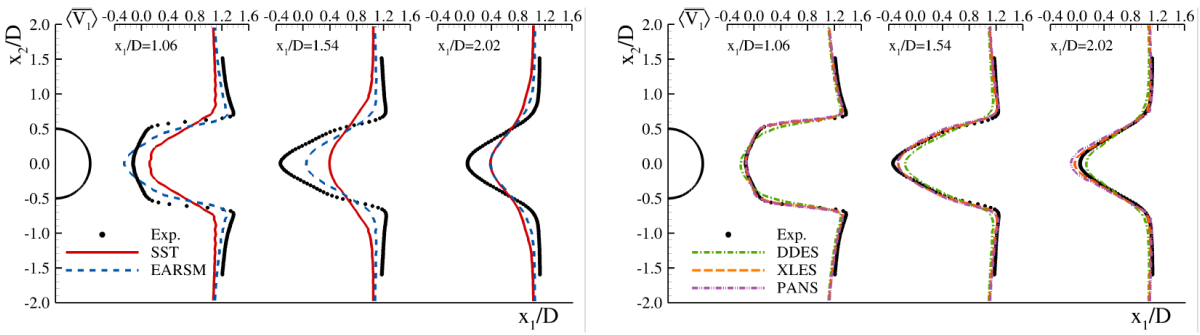

(a) $\langle \overline{V_1} \rangle$ - RANS models. (b) $\langle \overline{V_1} \rangle$ - SRS models.

Figure 23: Time-averaged stream-wise velocity downstream as function of turbulence model, $Re = 3\ 900$. Figure 2 in Vaz et al. (2017)

simulations show that the isotropic SST $k - \omega$ is unable to calculate these flows accurately. In comparison to the SST $k - \omega$ model, the EARSM model results in considerable improvements, as can be seen in table 2 (Vaz et al., 2017). The hybrid methods show a further leap in accuracy, and the results are in very good agreement with experiments for the circular cylinder. In figure 23, the improvement in accuracy for more sophisticated models is illustrated. The improvement in accuracy brings a significant increase in computing time, and this is summarized in table 6 (Vaz et al., 2017). For the square prism, there are also some discrepancies for the hybrid methods. The authors identify a need for further investigation of the square rounded prism, in order to identify model deficiencies. That effort is a part of a bigger set of verification studies, which is led by the development team behind the aforementioned ReFRESCO software package. This is a dedicated marine CFD tool, which is currently under development at mainly MARIN in the Netherlands.

Robertson et al. (2015) did a comparative study of turbulence models in OpenFOAM of the RANS and hybrid RANS/LES types. Three different test cases were used: flow over backward facing step, a sphere in the supercritical regime and a delta wing with a sharp leading edge. Among the RANS models, SST $k - \omega$ is found to be the most accurate. For hybrid methods, Spalart Allmaras - based DES model performed somewhat better than the $k - \omega$ based SAS model. As a sidenote, this study also identified which numerical schemes that are the most accurate and costly for the given type of turbulence model (RANS or hybrid). This is not relevant for this literature review, but highly relevant for performing efficient analyses in OpenFOAM of highly separated turbulent flows.

7.3 Discussion and Recommendations

In Larsson et al. (2014), it is noted that an isotropic turbulence model seems to be inadequate to model 3D separating flows. This is verified in Eça et al. (2017) and van Raemdonck et al. (2016), where the isotropic models SST $k-\omega$ and realizable $k-\epsilon$ performs poorly. This is further confirmed in Pereira et al. (2017), where 11 isotropic models are tested. However, these studies also show that when determining the total drag off a body with a large length/breadth-ratio (e.g. ships and trucks), an isotropic model is quite accurate. Boundary layers with limited curvature is accurately predicted, as these models have been tested and developed extensively for these types of flows. In this case, the assumption of an isotropic eddy viscosity seems to be accurate. The studies indicate that the SST $k-\omega$ model is the most accurate among the isotropic models.

Larsson et al. (2014) and Pereira et al. (2017) show that the anisotropic RANS model EARSM is a good alternative to isotropic RANS models for curved, separating flows. A significant increase in accuracy is achieved by a relatively small increase in computing cost. I.e., algebraic expressions for the anisotropy tensor needs to be computed and the iterative convergence is somewhat slowed down. The model performs worse than the isotropic models for the aforementioned total resistance predictions. Hence, among RANS models, EARSM should be used for separating flows, while isotropic models are better suited to predict boundary layers with limited curvature.

In terms of accuracy, the next level of modelling is the DES and SAS models. With RANS behaviour in attached boundary layers and LES behaviour elsewhere, these models optimally achieve LES accuracy without having to resolve a boundary layer with LES-resolution. This implies a significant reduction in computing cost compared to LES. Wu et al. (2016), Serre et al. (2013) and Vaz et al. (2017) show that these models can achieve accurate results for 3D highly separating flows. However, these models show inconsistencies and needs to be further evaluated. E.g., the RANS-LES switch needs to be improved (Moussaed et al., 2014). Thus, these models show promise but need further development and validation.

Comprehensive LES and DES simulations were performed in Serre et al. (2013). A further increase in accuracy is observed with LES, but at a considerable cost. If this is due to the RANS simulations in DES or because of algorithmic issues with DES, is an open question. Deficiencies with the LES simulations were found and further development needs to be performed for LES applied to 3D high Reynolds number separating flows.

The above may be summarized in the following:

- Isotropic RANS models are unable to predict high Reynolds number separating flows, but is a cheap and quite accurate option for boundary layers with limited curvature.
- The anisotropic RANS model EARSM yields a big improvement in the calculation of 3D separating flows compared to isotropic RANS models.
- DES and the SAS models provide accurate predictions for complex 3D separating flows, but are not well validated and show some inconsistencies. Further development and validation is needed.
- LES simulations provide accurate results, but are presently too computationally expensive for engineering purposes. LES has the inherent problem of a very fine boundary layer resolution, but its cost may be reduced by algorithmic/modelling improvements.

Thus, for engineering purposes, I recommend EARSM, DES and SAS models for turbulence modelling of flows around bluff bodies at high Reynolds number. The former do only increase the computational cost slightly from isotropic RANS models. The two latter are more costly, but have produced highly accurate results for complex flows. All of the three models need further development and validation, but the preliminary results looks promising.

8 Conclusions

The objectives of the 2D simulations, given in section 1.1.1, involve grid generation, post-processing and the use of OpenFOAM. A natural quality measure of the simulations is the comparison of C_D, C_L and St with references. Additionally, visualization and assessment of various flow features are in line with the above. During the work with the 2D simulations, I have gained basic grid generation and post-processing skills. By working with OpenFOAM, I have become well acquainted with its basic usage and default numerical routines. It has also teached me a procedure for developing grids: determination of boundary layer resolution, domain size and temporal discretization. The results of the primary variables are within 2-3% of the reference values, indicating decent grid generation and post-processing. However, a significant deviation from references was observed with the reattachment angle, illustrating deficiencies in the mesh design and/or numerical schemes. In general, the literature review could have been more extensive, such that more definitive values for the variables of interest had been found. This would in turn made an assessment of the results clearer. However, I think the basic objectives of this project concerning grid generation, post-processing and basic OpenFOAM usage have been achieved through the 2D simulations.

The 3D simulations were performed with artificial boundary conditions, resulting in an unphysical flow. Hence, the quantitative results from this study are of limited usage; the vortex dynamics were fundamentally altered, yielding large deviations in St and C_L'. But more importantly for this project, the flow proved to be three-dimensional and I was able to gain some post-processing experience with 3D separating flows. The lambda2 method was used to investigate the temporal and spatial evolution of coherent structures. Further, the pressure in these structures were examined. The correlation length of structures at the cylinder mid-span was found to be close to references. Similarly as in 2D, the primary objectives concerning post-processing have been achieved in the 3D simulations. Contrary to the 2D case, the pre-processing was less extensive. In a comprehensive study of the 3D cylinder, first a grid generation procedure as performed in 2D should have been perfromed. First and foremost a larger domain in z-direction would be needed to ensure physical boundary conditions. Next, a more comprehensive grid convergence study would limit discretization errors and provide results of quantitative use.

The literature review provided some distinct results. Popular two-equation models seems to be unable to predict the flow around bluff bodies at high Reynolds numbers. EARSM, DES and SAS were identified as promising engineering models for these types of flows. In numerous studies, they have predicted complex, highly separating flows with high accuracy. Nevertheless, these models need further development and validation efforts. Some inconsistencies with these models were noted, but an in-depth analysis of the model features are outside the scope of this review. Presently, LES seems to be too computationally costly for engineering purposes due to the very fine resolution needed in the boundary layer for high Reynolds number flows.

9 Further Work

The first step towards improving the 2D study would be a more comprehensive literature review. Next, a thorough convergence study would result in more accurate estimates of the primary and secondary flow variables. Additionally, a more in-depth investigation of secondary flow structures could be pursued; something left untouched in this study is the vortex dynamics downstream in the wake. Conclusively, the study of the circular cylinder at $Re = 100$ is far from completed after this study.

The major steps towards improving the 3D study is given in the previous section. I.e., more extensive pre-processing and a critical assessment of the resulting more realistic results. In a more general view, thinking of my master's thesis in spring, I can do some elaboration.
Regarding pre-processing, I need to work more with 3D pre-processing, as this was very limited in the 3D simulations. I.e., grid generation as performed for the 2D grid. However, I expect that many of the approaches used in 2D may be extended to 3D. Additionally, a formal grid convergence study should be conducted (Wang et al., 2008). Regarding OpenFOAM usage, I have still just scratched the surface of its capabilities and different numerical schemes. A more thorough investigation of OpenFOAM is needed during the master thesis work, where the more advanced problem requires more in-depth OpenFOAM proficiency. In that regard, turbulence modelling is a keyword and Robertson et al. (2015) will work as a good starting point. I have gained some 3D post-processing experience through the 3D simulations. However, also in this area more sophisticated use is needed in the master thesis. I.e., to investigate the evolution of coherent flow structures and to identify prominent wake modes more accurately.

The literature review narrowed down the suitable types of turbulence models for high Reynolds number flows around bluff bodies. EASRM is a relatively cheap alternative computationally, while DES and SAS are more costly. If these models are to be used during the master thesis work, I need a thorough understanding of these methods. I.e., a good theoretical understanding and to perform a more comprehensive literature review to identify known deficiencies. As these models are still in the development phase, at least the two latter ones, such an understanding is necessary to critically assess results. Due to time limitations, this was not pursued in this work. In addition, I need to assess the numerical performance of the above models in OpenFOAM, and to that end Robertson et al. (2015) is a good starting point.

Conclusively, in the 2D and 3D simulations, I have obtained a decent background in pre-processing, post-processing and OpenFOAM usage. Nevertheless, during the master thesis I will need to further improve these skills and learn how to conduct a proper convergence study. This needs to be addressed alongside a better theoretical understanding of the above identified turbulence models and knowledge about their deficiencies and efficiency in OpenFOAM.

References

B. N, R., Gopal Lanka, H., and Majumdar, S. (2017). *Laminar flow past a circular cylinder at reynolds number varying from 50 to 5000.* Technical Report. National Aerospace Laboratories, Bangalore, India.

Drazin, P. G. (2002). *Introduction to hydrodynamic stability.* Cambridge Univ. Press, Cambridge [u.a.], first edition. (pp. 139-145).

Eça, L., Vaz, G., Koop, A., Pereira, F., and Abreu, H. (2017). Validation exercises for the calculation of the flow around a squared column with rounded corners at high reynolds numbers with the rans equations. *ASME 2017 36th International Conference on Ocean, Offshore and Arctic Engineering*, (57649):V002T08A015.

Irgens, F. (2008). *Continuum mechanics.* Springer, Berlin, first edition. (pp. 50-55, 199-204).

Jasak, H. (2015). Finite volume discretisation in openfoam best practice guidelines. url: `www.tfd.chalmers.se/~hani/kurser/OS_CFD_2015/HrvojeJasak/DiscretisationBestPractice.pdf`.

Jeong, J. and Hussain, F. (2006). On the identification of a vortex. *Journal of Fluid Mechanics*, 285:69–94.

Kolmogorov, A. N. (1941). The local structure of turbulence in incompressible viscous fluid for very large reynolds numbers. *Proceedings of the USSR Academy of Sciences*, 30:299–303.

Kundu, P. K., Cohen, I. M., and Dowling, D. R. (2012). *Fluid mechanics with Multimedia DVD.* Academic, Amsterdam; London, fifth edition. (pp. 99-115).

Larsson, L., Stern, F., and Visonneau, M. (2014). *Numerical Ship Hydrodynamics An assessment of the Gothenburg 2010 Workshop.* (pp. 1-2. 9-11, 65-84).

Menter, F. R. and Egorov, Y. (2010). The scale-adaptive simulation method for unsteady turbulent flow predictions. part 1: Theory and model description. *Flow, Turbulence and Combustion*, 85(1):113–138.

Moussaed, C., Vittoria Salvetti, M., Wornom, S., Koobus, B., and Dervieux, A. (2014). Simulation of the flow past a circular cylinder in the supercritical regime by blending rans and variational-multiscale les models. *Journal of Fluids and Structures*, 47:114–123.

Müller, B. (2017). *Lecture notes for the course TEP4165 Computational Heat and Fluid Flow, NTNU Trondheim.* (pp. 10, 24-25).

Norberg, C. (2001). Flow around a circular cylinder: Aspects of fluctuating lift. *Journal of Fluids and Structures*, 15(3):459–469.

Pereira, F. S., Eça, L., and Vaz, G. (2017). Verification and validation exercises for the flow around the kvlcc2 tanker at model and full-scale reynolds numbers. *Ocean Engineering*, 129(Supplement C):133–148.

Prandtl, L. (1904). Über flussigkeitbewegung bei sehr kleiner reibung [english translation in naca technical memo. 452]. *Proc. Third Int. Math. Congr. Heidelbwerg.*

Rajani, B. N., Kandasamy, A., and Majumdar, S. (2009). Numerical simulation of laminar flow past a circular cylinder. *Applied Mathematical Modelling*, 33(3):1228–1247.

Robertson, E., Choudhury, V., Bhushan, S., and Walters, D. K. (2015). Validation of openfoam numerical methods and turbulence models for incompressible bluff body flows. *Computers and Fluids*, 123:122–145.

Roshko, A. (1954). On the development of turbulent wakes from vortex streets. Technical report. naca 1191.

Schlichting, H., Gersten, K., Krause, E., and Oertel, H. (2017). *Boundary-layer theory.* Springer, Berlin, ninth edition. (pp. 145-155, 340).

Serre, E., Minguez, M., Pasquetti, R., Guilmineau, E., Deng, G. B., Kornhaas, M., Schäfer, M., Fröhlich, J., Hinterberger, C., and Rodi, W. (2013). On simulating the turbulent flow around the ahmed body: A french-german collaborative evaluation of les and des. *Computers and Fluids*, 78:10–23.

Sumer, B. M. and Fredsøe, J. (1997). *Hydrodynamics around cylindrical structures.* World Scientific Publishing, London, first edition. (pp. 1-11).

van Raemdonck, G. M. R., van Leeuwen, P., and van Tooren, M. J. L. (2016). Comparison of experimental and numerically obtained flow properties of a bluff body. 79:393–411.

Vaz, G., Pereira, F., and Eça, L. (2017). On the prediction of shear-layer flows with rans and srs models.

Versteeg, H. K. and Malalasekera, W. (2007). *An introduction to computational fluid dynamics : the finite volume method.* Pearson Education, Harlow. (pp.187-193, 267-275, 281-284).

Wang, S. Y., Yafei, J., A. Schmalz Jr., R., J. Roache, P., and Smith, P. (2008). *Verification and Validation of 3D Free-Surface Flow Models.* American Society of Civil Engineers / ASCE. (pp. 31-34).

White, F. M. (2007). *Viscous fluid flow.* McGraw-Hill, Boston [u.a.], third edition. (pp. 230-232).

Wilcox, D. C. (2006). *Turbulence modeling for CFD.* DCW Industries, La Cañada, Calif. (pp. 15-17, 34-43, 57-58, 122-130, 311-315, 371-372, 436-440).

Wu, C. H., Ma, S., Kang, C. W., Lim, T. B. A., Jaiman, R. K., Weymouth, G., and Tutty, O. (2016). Vortex-induced motion of a square cylinder at moderate reynolds numbers. *Proceedings of the International Conference on Offshore Mechanics and Arctic Engineering - OMAE*, 2.

Zheng, W., Yan, C., Liu, H., and Luo, D. (2016). Comparative assessment of sas and des turbulence modeling for massively separated flows. *Acta Mechanica Sinica/Lixue Xuebao*, 32(1):12–21.

Çengel, Y. A. and Cimbala, J. M. (2013). *Fluid mechanics : fundamentals and applications.* McGraw-Hill Education, New York, NY, third edition. (pp. 579 , figure 11-25).

10 Appendix

10.1 Miscellaneous Discussions

Mechanism of secondary flow feature due to reattachment
I assume the vortex in figure 14a obtains vorticity from reattachment of the main vortex on its side. Simultaneously, it will be pushed towards the other side of the cylinder(b), due to the main vortex shedding mechanism (cf. section 2.3). At (c), the vortex is halted due to counteracting vorticity from a reattached vortex equivalent to that one in (a). Now, this vortex behaves as explained in (a)-(c) in the opposite direction. This phenomena will both effect the main vortex on its original side and the opposite. In (b) one see that it has a significant size, and thus counteracts and pushes the main vortex downstream. In (c), it strengthens the opposite main vortex and pushes it downstream. Due to the symmetry of this mechanism, I assume it to be periodic with approximately $2f_v$. This is also seen in figure 12, where the second most important frequency is close to $2f_v$.

Boundary layer development from 2D to 3D
If one assumes boundary layer theory is valid for this flow at $\theta = 60°$, equation (7) may be used to assume the relation

$$\delta = \frac{C}{\sqrt{Re}} \qquad C \in \mathbb{R} \tag{34}$$

Then, given the boundary layer thickness for $Re = 100$ and the above relation, boundary layer theory would predict $\delta = 0.17$ for $Re = 300$. Note, the actual value is approximately 0.19. Even though the flow is highly curved (a violation of boundary layer theory), boundary layer theory yields quite a good approximation.

CPU time development from 2D to 3D
The increase in mesh size from the 2D simulations is a factor of approximately 29. The most restrictive procedure in FVM codes for large simulations is the iterative solution of the linear system of equations for the pressure corrections. In this simulation, the multigrid method GAMG is used and in general multigrid methods has linear convergence properties (B. Müller, personal communication, October 19, 2017). Hence, the increase in the computing metric q should equal 29 if the above is to hold. As this is roughly 80, other factors are also important. I.e., other solution step procedures as the effect of artificial boundary conditions and/or hardware limitations. In the 2D simulations the simulations were run on a single core, while they were run on four cores in 3D. The parallellization may reduce the computing performance on a per processor basis.

10.2 OpenFOAM Boundary and Initial Conditions

In the following, boundary and initial condition treatment in OpenFOAM is summarized. I will only present those aspects relevant to the 2D and 3D simulations.

Every boundary needs to be assigned an OpenFOAM "type". The "type" of the boundary determines, which boundary conditions that may be applied. Below, I have presented the types used in the simulations. This information is inserted into the run directory in constant/polyMesh/boundary.c

patch Type suited for inlets and outlets. Both fixed values(Dirichlet) and gradients (Von Neumann) may be applied.
zeroGradient This type is exclusively used to apply the zero gradient condition. It is suitable for boundaries crosswise to the flow direction.
wall The wall type is used at walls to enforce no-slip and impenetrability on the velocity field and zeroGradient on the pressure (cf. section 2.8).
empty This is a boundary used in 1D or 2D flows, where boundaries normal to the flow direction are excluded from the simulation.

Table 7: Type definitions in OpenFOAM v1706

Following the type definitions, the boundary conditions to p and U(vector) is prescribed in the 0 folder. Here each variable needs to be assigned a type similar to the above. In the cases of wall, empty and zeroGradient, no further information is needed. In the case of the type fixedValue, also the value(s) has to be specified. Regarding initial conditions, these are also specified in the 0 folder.

10.3 Boundary Layer Profiles Task A

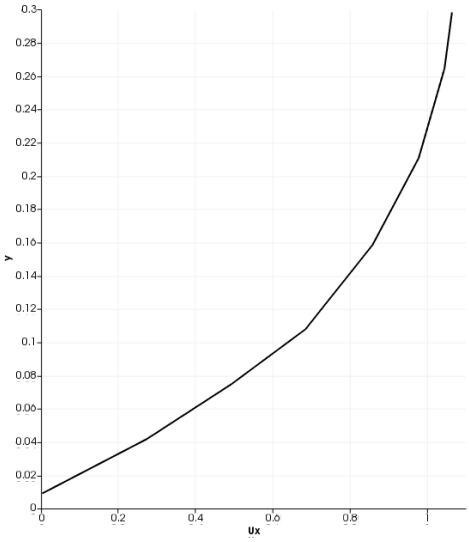

(a) $N = 3$

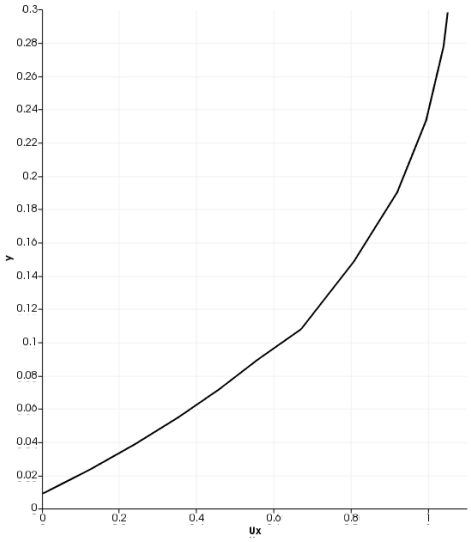

(b) $N = 6$

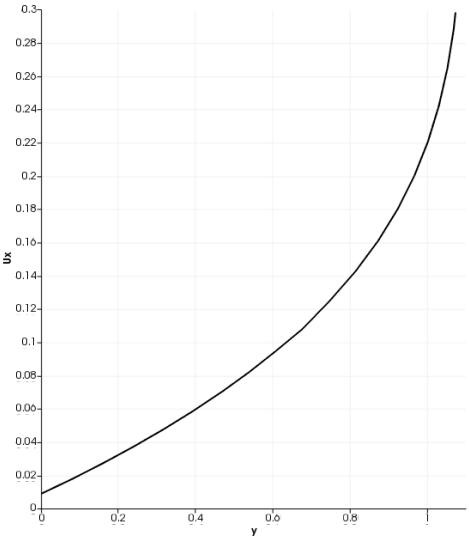

(c) $N = 9$

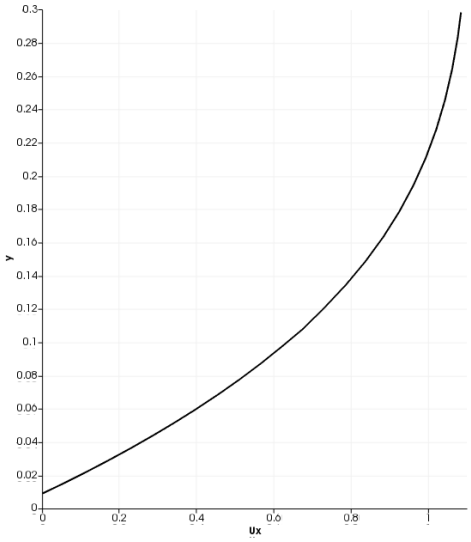

(d) $N = 12$

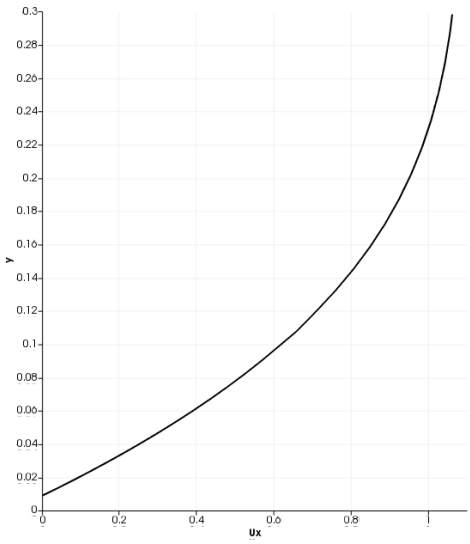

(e) $N = 15$

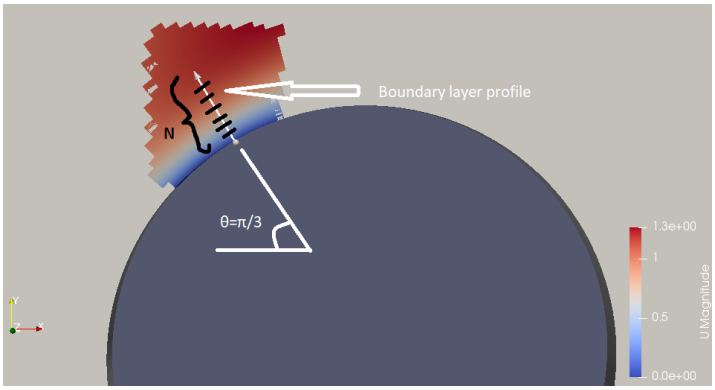

(f) Location of profiles

Figure 24: Boundary layer profiles task A

10.4 Top Boundary Streamwise Velocity Task B

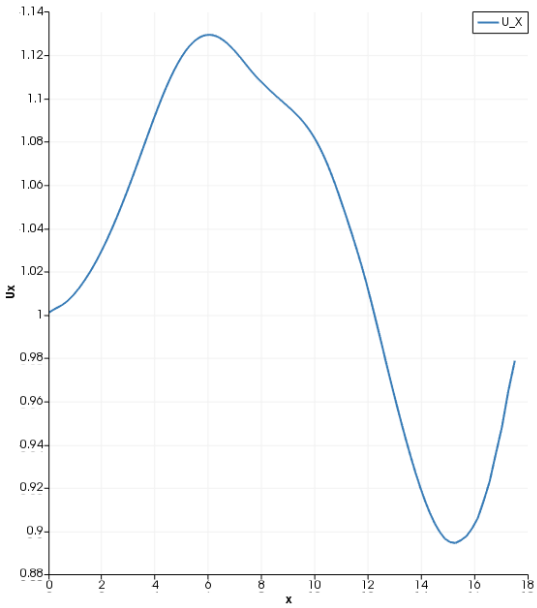

(a) $\alpha = 2.5$

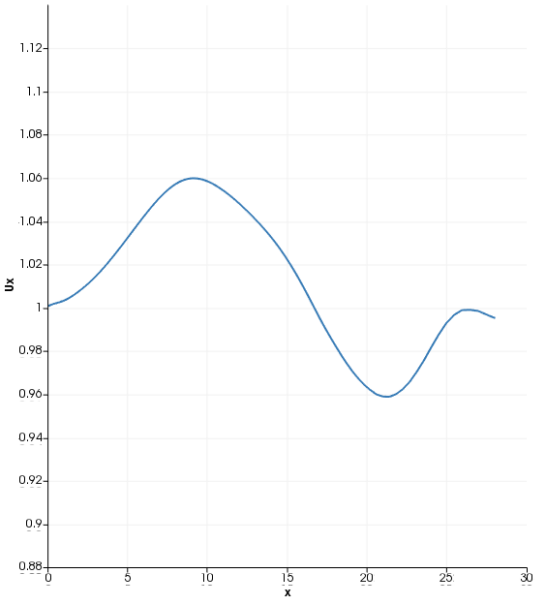

(b) $\alpha = 4$

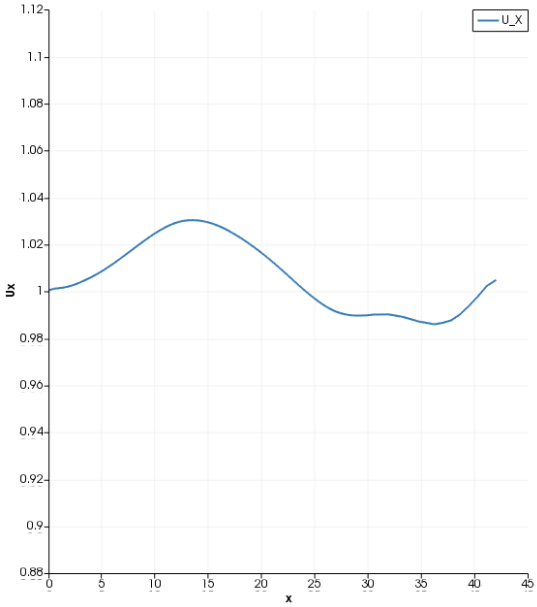

(c) $\alpha = 6$

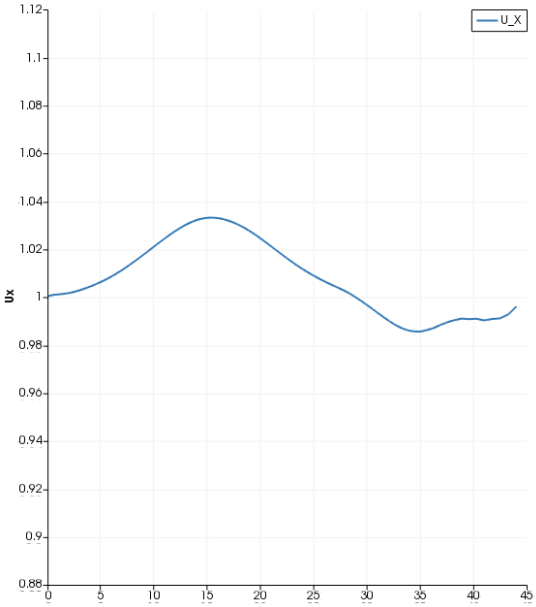

(d) $\alpha = 7$

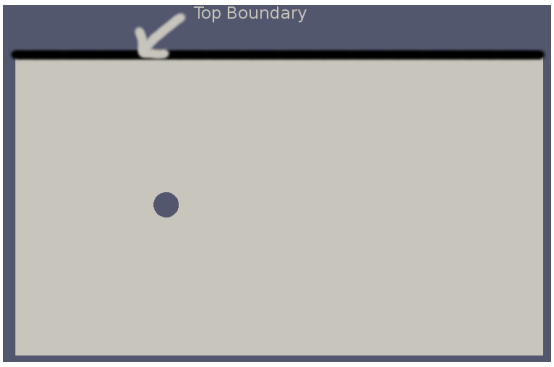

(e) Location of top boundary, $y = \alpha D = 2\alpha$

Figure 25: Streamwise velocity at top boundary task B

10.5 Pressure Contours Task C

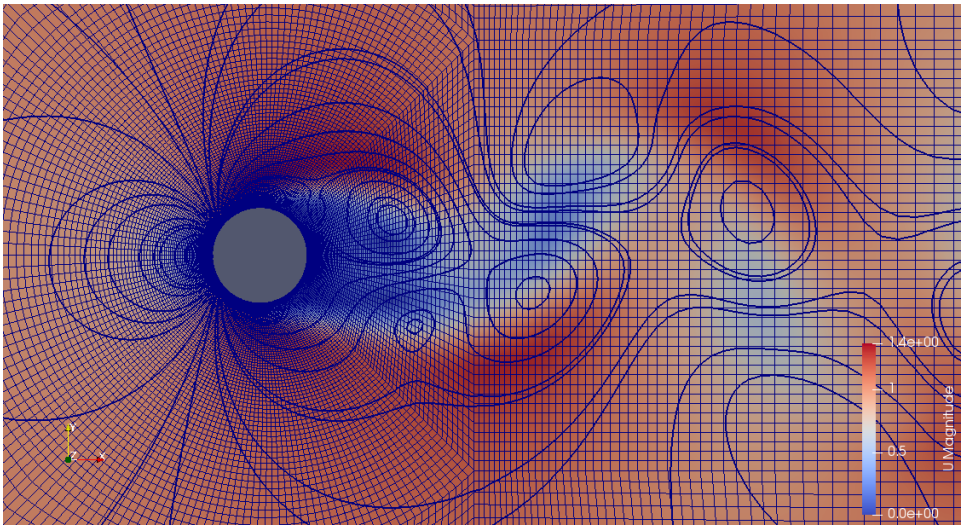

(a) Critical C-mesh areas

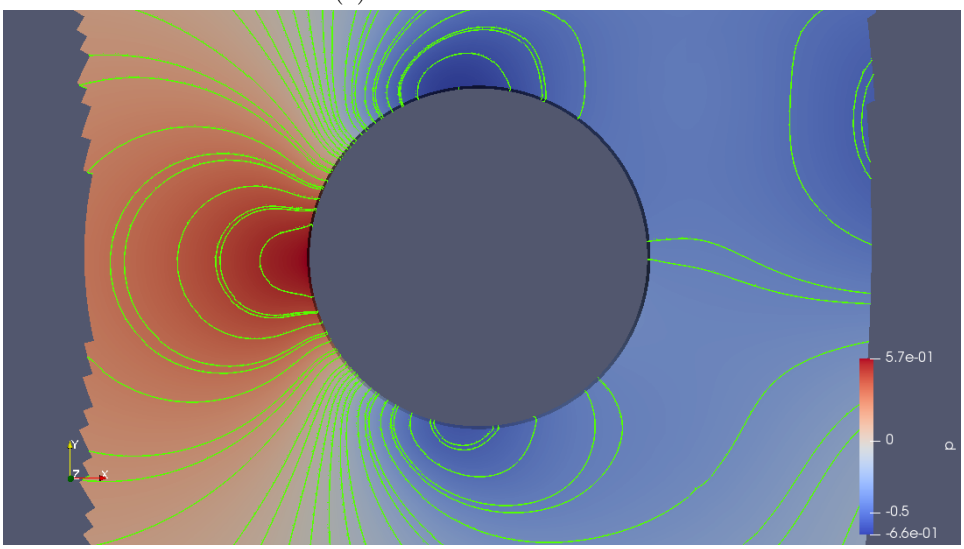

(b) Boundary layer

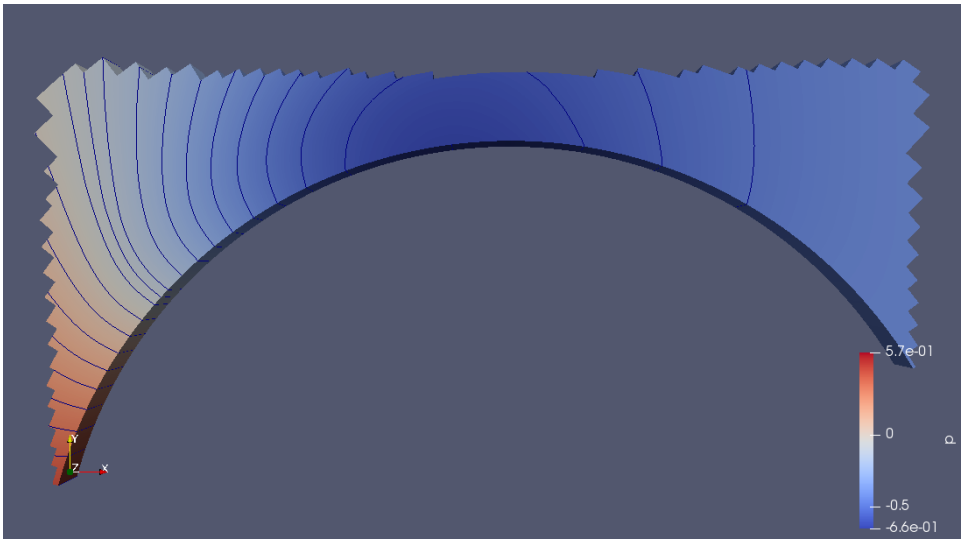

(c) Boundary layer close-up

Figure 26: Pressure contours task C

10.6 Final Grid Task C

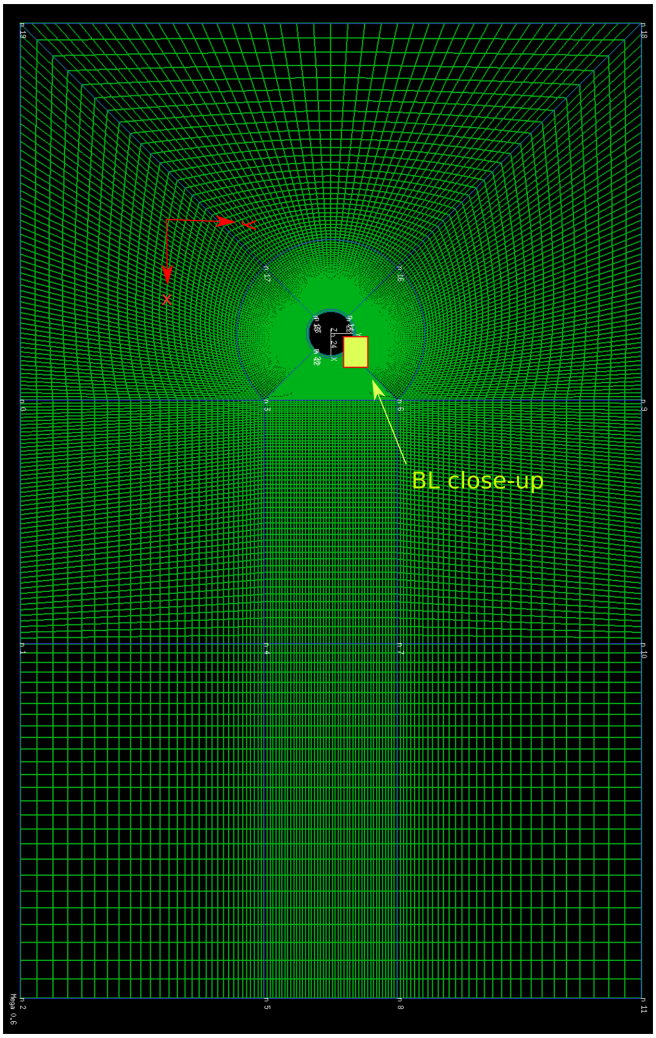

Figure 27: Final grid task C

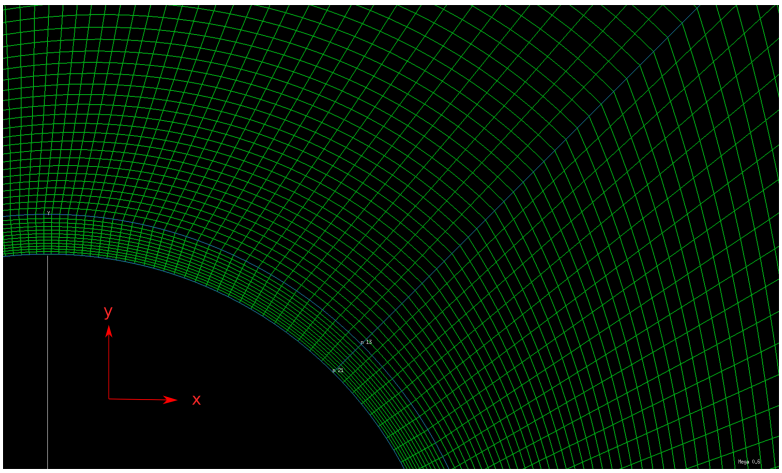

Figure 28: Boundary layer close-up of final grid

10.7 Mesh Verification Step 1

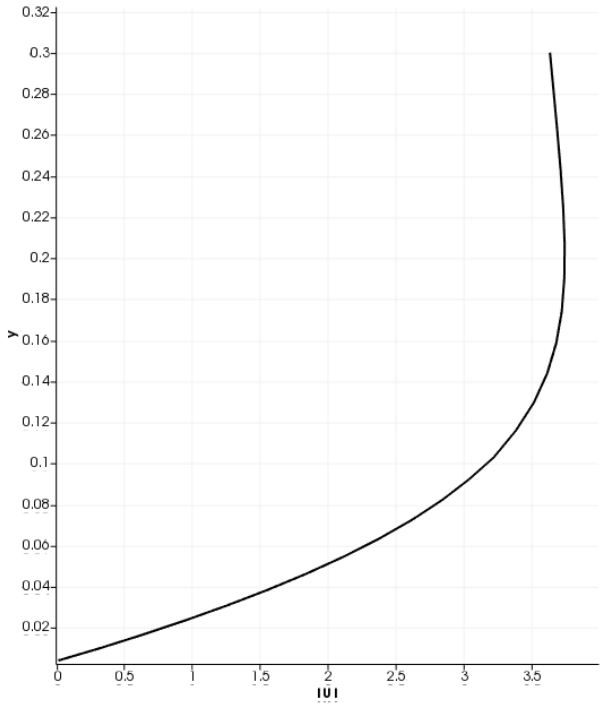

(a) Boundary Layer: $N = 12$, $\theta = 60°$

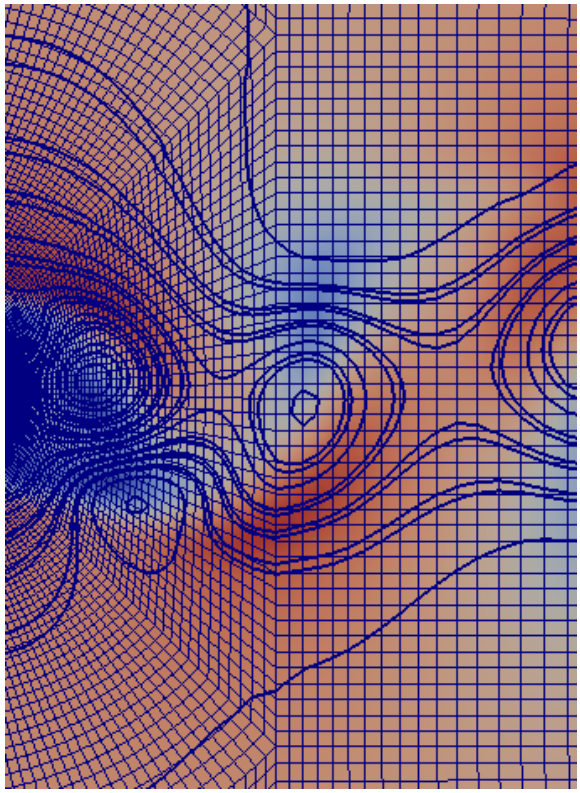

(b) Pressure contours

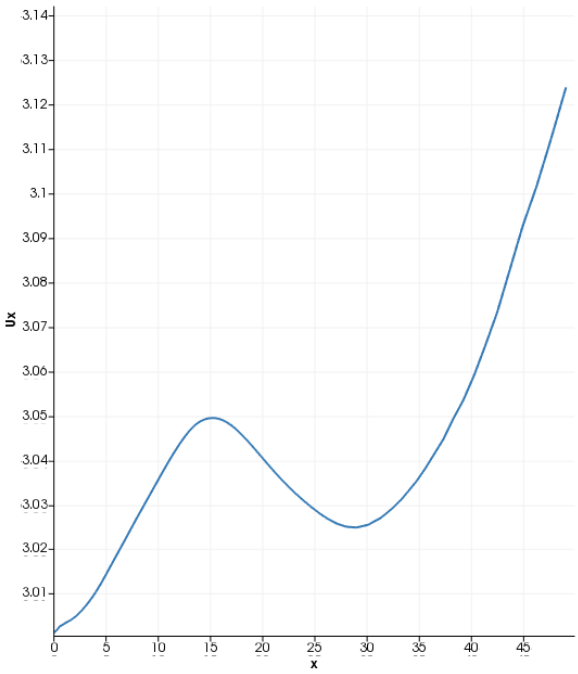

(c) Streamwise velocity at top boundary, $y = 14$

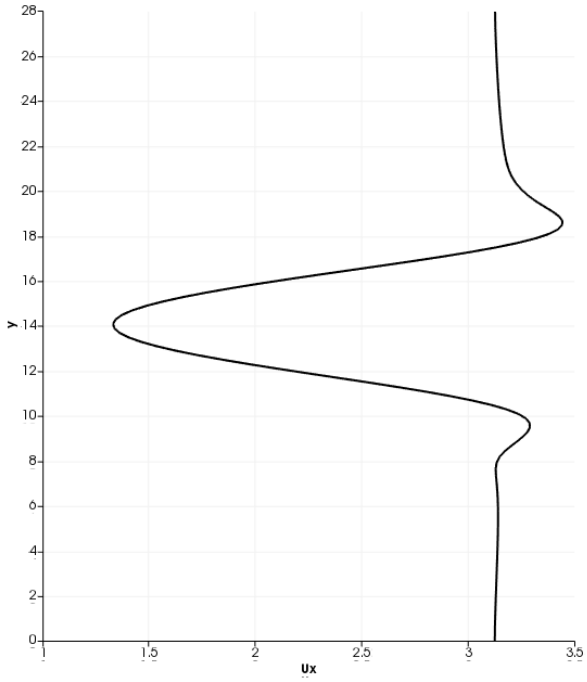

(d) Streamwise velocity at outlet boundary, $x = 35$

Figure 29: Mesh verification step 1

10.8 Postprocessing Script post.py


```python
import numpy as np
import matplotlib.pyplot as plt
import operator
import os
import csv



## --- Functions --- ##

def forceCoeffs(NT):
    '''
    Load Cl and Cd data from wanted time instance
    '''

    # Open file
    root = os.getcwd()
    os.chdir('/home/henrik/Documents/Prosjekt/Ex3/run/postProcessing/forceCoeffs/0')
    list = os.listdir(os.getcwd())

    if len(list)>1:
        print 'Only one dat file!'
        return
    else:
        CdCl = np.genfromtxt(list[0],skip_header=9,dtype=float)
    N = len(CdCl[:,1])


    # Load Cd, Cl and time
    Tt = CdCl[N-NT:,0]
    Cd = CdCl[N-NT:,2]
    Cl = CdCl[N-NT:,3]

    # Change directory back to default
    os.chdir(root)

    # Return Cd, Cl and time
    return Cd, Cl, Tt



def pressure(NT,N):

        """
        Load  desired pressure data
        """

        # Open file
        root = os.getcwd()
        os.chdir('/home/henrik/Documents/Prosjekt/Ex3/run/postProcessing')

        with  open('pc050.csv','r') as csvfile:
        data = csv.reader(csvfile)

        # Read data
        p = []
        i = 1
        for row in data:

            if i ==1 or i==2:
                pass
            elif i < N-NT:
                pass
            else:
```

```
                    p.append(float(row[6]))
                i+=1

            # Change directory back to default
            os.chdir(root)


            # Return p
            return p




## --------- Program post --------- ##




## Force coefficients


# User input - interesting time interval and dt
dt = 0.005
Tstart = 170
Tend   = 200
WT = 70  # write interval

# Timestepping varialbles
DT = WT*dt
nt = int(round((Tend-Tstart)/dt))
NT = int(round((Tend-Tstart)/DT))
n = int(Tend/dt)
N  = int(Tend/DT)

# Load Cl, Cd and time data
Cd, Cl, Tt = forces(nt)


# Rms of Cd, Cl
n = len(Cd)
Cd_rms = np.sqrt(np.sum(np.power(Cd,2))/n)
Cl_rms = np.sqrt(np.sum(np.power(Cl,2))/n)


# Force coefficient amplitudes
Cd_max = max(Cd)
Cd_min = min(Cd)
Cl_max = max(Cl)

# Dynamic drag coefficient
Cd_d = (Cd_max-Cd_min)/2
# Steady drag coeffiecient
Cd_s = Cd_max-Cd_d


# Print results to screen
print 'Cd_max = ' , Cd_max
print 'Cd_rms = ',
print("%3.7f"% (Cd_rms))
print 'Cd_s   = ', Cd_s
print 'Cd_d   = ', Cd_d
print 'Cl_max = ', Cl_max
print 'Cl_rms = ',
print("%3.7f"% (Cl_rms))
```

```python


# Plotting of Cd and Cl
t = np.linspace(Tstart,Tend,nt)
fig = plt.figure(1)
fig.suptitle('Drag and lift coefficients', fontsize=16, fontweight='bold')
ax =fig.add_subplot(111)
ax.set_xlabel('$t$',fontsize=14)
ax.set_ylabel('$C_D , C_L$',fontsize=14)
plt.plot(t,Cd,label='$C_D$')
plt.plot(t,Cl,label='$C_L$')
line_cd, = plt.plot(t,Cd.real,label='$C_d$')
line_cl, = plt.plot(t,Cl.real,label='$C_l$')
plt.legend(handles=[line_cd,line_cl])
plt.grid()
plt.savefig('figures/cdcl.png',dpi=72)





##  Frecuency analysis
p = pressure(NT,N) # get p in time domain

p_omega = np.fft.fft(p) # FFT of p
freq = np.linspace(0.0,1.0/(2.0*DT),NT/2) # Corresponding frequencies
p_omega = 2.0/NT*np.abs(p_omega[0:NT/2]) # 1-sided, real spectrum

# Time discretisation
n=len(p)
t = np.linspace(Tstart,Tend,n)

# Plotting of p in frequency and time domain
fig = plt.figure(2)
fig.suptitle('Pressure', fontsize=16, fontweight='bold')
ax =fig.add_subplot(211)
ax.set_xlabel('$f$',fontsize=14)
ax.set_ylabel('$p$',fontsize=14)
plt.plot(freq,p_omega,label='$p(\omega)$')
plt.grid()
ax =fig.add_subplot(212)
ax.set_xlabel('$t$',fontsize=14)
ax.set_ylabel('$p$',fontsize=14)
plt.plot(t,p,label='$p(t)$')
plt.grid()
plt.savefig('figures/p.png',dpi=72)
plt.show()
```

List of Figures

1 Energy spectrum of turbulent flow in log-log scales, figure 2.15 from Müller (2017) . 1
2 Boundary layer development (Çengel and Cimbala, 2013) 4
3 Von Kármán vortex street $Re = 100$, $\sqrt{\omega_i \omega_i}$ 5
4 Vortex shedding as depicted in figure 1.7 in Sumer and Fredsøe (1997) 5
5 Time averaging of nonstationary turbulence (Wilcox, 2006) 6
6 Flow domain 2D 10
7 Mesh topology 2D 11
8 Reference figures from Norberg (2001) 14
9 Reference figures from Rajani et al. (2009) 15
10 Separation and reattachment points 17
11 Final boundary layer profile, top streamwise velocity and top boundary location . . . 17
12 Pressure output task D 18
13 Drag and lift coefficients task D 18
14 Vorticity magnitude time series task D 19
15 Vorticity-pressure plot task D 19
16 Mesh after step 2 21
18 Top-down view of λ_2 22
17 Temporal evolution of flow structures, λ_2 method 22
19 Spatial evolution of flow structures 23
20 Pressure - λ_2 interdependence 24
21 Rear pressure distributions in van Raemdonck et al. (2016)) 29
22 Vortex structures visualized by iso-surfaces(Q-criterion, Q = 60): (a) DES-SST, (b) LES-NWR, (c) LES-SVV (Figure 6 in Serre et al. (2013)) 31
23 Time-averaged stream-wise velocity downstream as function of turbulence model, $Re = 3\ 900$. Figure 2 in Vaz et al. (2017) 31
24 Boundary layer profiles task A 39
25 Streamwise velocity at top boundary task B 40
26 Pressure contours task C 41
27 Final grid task C 42
28 Boundary layer close-up of final grid 42
29 Mesh verification step 1 43

List of Tables

1 Initial- and boundary conditions 2D 11
2 Primary variables task B 16
3 Primary variables and CFL task C 16
4 Configuration in task D 16
5 Results task D 16
6 Primary variables 3D simulation 20
7 Type definitions in OpenFOAM v1706 38